Volume 20
DOE/DP40124-46

LLE Review

Quarterly Report

July–September 1984

Laboratory for Laser Energetics
College of Engineering and Applied Science
University of Rochester
250 East River Road
Rochester, New York 14623

Volume 20
DOE/DP40124-46

LLE Review

Quarterly Report

Editor: L. Iwan
(716) 275-5101

July–September 1984

Laboratory for Laser Energetics
College of Engineering and Applied Science
University of Rochester
250 East River Road
Rochester, New York 14623

IN BRIEF

This volume of the LLE Review contains articles on the activities in the GDL and OMEGA laser facilities, some design changes to be implemented on the OMEGA laser, techniques for estimating UV target-irradiation uniformity, progress in fabricating polymer-shell targets, refined estimates of thermal electron transport in IR-irradiated targets, a program to develop a surgical instrument to excise arterial blockages with a laser, a new damage criterion for optical coatings, and NLUF activities for July–September 1984.

Some highlights of these articles are

- A new front end has been designed for OMEGA. Improved beam-profile control is incorporated into the configuration, and there is sufficient additional gain to implement fully active, mode-locked, Q-switched oscillators.
- We continue to extend our capabilities to estimate target-illumination uniformity. Reduction of equivalent-target-plane photographs is carried out with a higher degree of automation, and the beam-superposition code now accommodates azimuthal as well as radial intensity variations.
- Microencapsulation techniques have been employed to fabricate target-quality microballoons with several polymers. Some materials have been selected on the basis of their physical properties for further development.

- Progress has been made in establishing values for the flux limiter and preheat limits. This was done by comparing experimental results for 24-beam, 1054-nm target experiments with implosions modeled with the code *LILAC*. The ring structure in the x-ray microscope images is quite sensitive to the values of the two parameters and is best replicated with the flux limit equal to 0.05 and 16% of the absorbed energy in suprathermal electrons.
- An argon-ion laser was shown to be more effective than Nd:YAG for destroying cholesteric deposits on the walls of animal and human arteries. This laser will be incorporated into a fiber-optic delivery system to carry out internal removal of arterial blockages in living animals and humans.
- A new engineering damage criterion is proposed for thin-film coatings. This criterion is the appearance of multiple damage sites in an irradiated area visible to the unaided eye. The old criterion — the appearance of even a single, often microscopic, scattering center — is less relevant for the evaluation of coatings in LLE laser systems.

CONTENTS

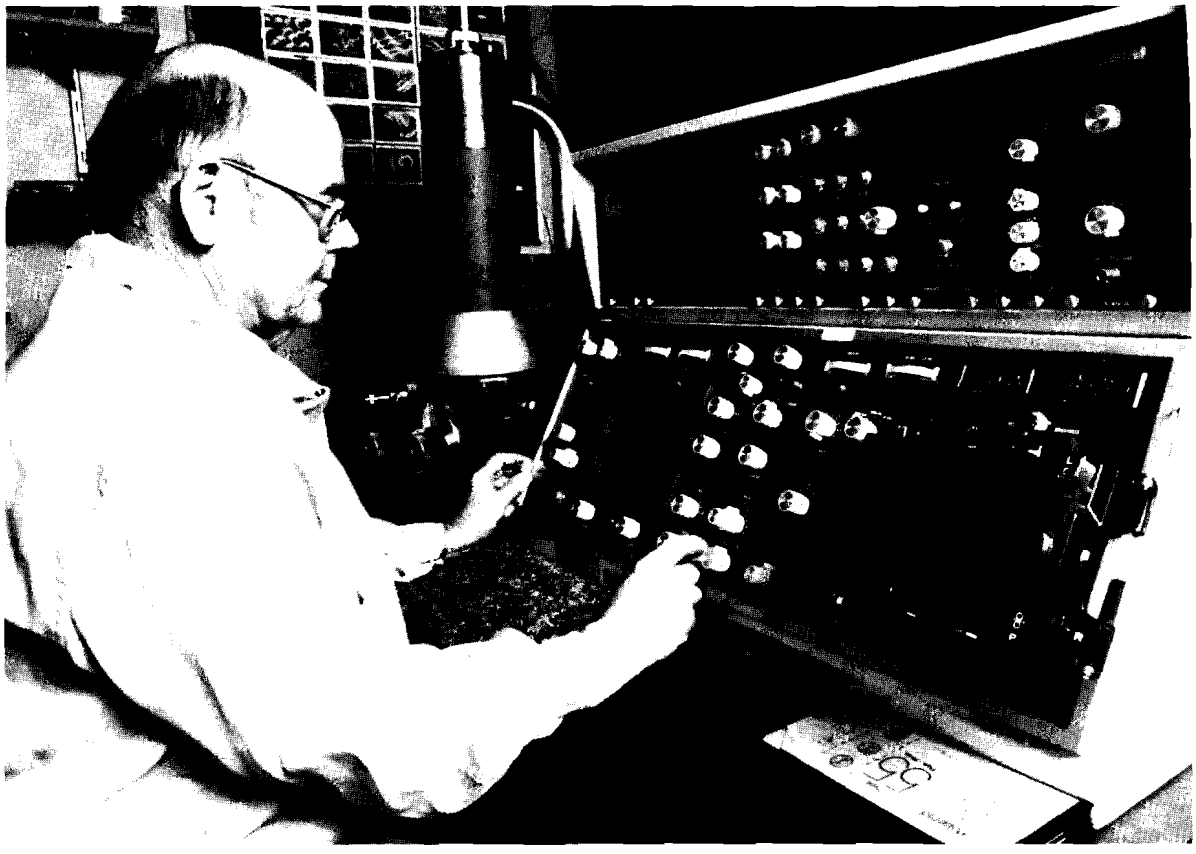

Luther Whitaker, senior technical associate in the Target Fabrication Group, prepares to photograph a microballoon with the scanning electron microscope (SEM). SEM photographs appear in this and other issues of the LLE Review.

Section 1
LASER SYSTEM REPORT

1.A GDL Facility Report

The glass development laser (GDL) was shut down for a substantial portion of the fourth quarter of this fiscal year after a series of shots for damage testing, liquid-crystal polarizer evaluation, x-ray studies, and user experiments in early July. This shutdown was planned in order to carry out changes necessary to implement the active mirror booster and to improve the layout for beamline alignment. During this period, operations personnel also upgraded the target area by installing a new focus lens on the target chamber and rerouting the beam paths in order to facilitate alignment. With the implementation of active mirrors on GDL, the system will incorporate for the first time a monolithic OMEGA-style conversion cell and the multi-wavelength energy-sensing system. GDL is scheduled for complete reactivation during the month of October.

A summary of GDL operations this quarter follows:

Interaction Shots		9
NLUF Shots (UCLA/Yale)		34
Damage-Testing Shots		96
Alignment, Test Shots		8
Liquid-Crystal Test Shots		28
	TOTAL	175

A summary of GDL operations for FY84 follows:

Interaction Shots	246
X-Ray Shots	147
Damage-Testing Shots	947
Alignment, Test Shots	196
TOTAL	1536

ACKNOWLEDGMENT

This work was supported by the U.S. Department of Energy Office of Inertial Fusion under contract number DE-AC08-80DP40124 and by the Laser Fusion Feasibility Project at the Laboratory for Laser Energetics which has the following sponsors: Empire State Electric Energy Research Corporation, General Electric Company, New York State Energy Research and Development Authority, Northeast Utilities Service Company, Ontario Hydro, Southern California Edison Company, The Standard Oil Company, and University of Rochester. Such support does not imply endorsement of the content by any of the above parties.

1.B OMEGA Facility Report

OMEGA operations during this quarter consisted of two brief experimental campaigns in July and then a temporary suspension of target experiments in order to complete the conversion of the next six OMEGA beams from the infrared (IR) to the ultraviolet (UV).

In early July, we spent a week converting the focusing geometry of OMEGA from circular to linear, to provide line focus on cylindrical targets with four of the six UV beams. We then carried out a set of target experiments, investigating cylindrical plasmas produced with the line-focused beams. The results were interesting, and we anticipate more of these experiments in the future.

In mid-July the operations group reconverted to circular focus geometry for a brief series of experiments. In the remaining single week, shots were taken to support a user experiment from the University of Hawaii, to conduct some LLE implosion studies, and to carry out additional high-Z plasma-dynamics experiments in collaboration with Los Alamos National Laboratory. A total of 40 shots were taken during the week of 16 July. After this series, the system was shut down for conversion. In the remainder of the quarter we converted the six-beam "A" group of OMEGA's 24 beams to the UV. In August the structures were put in place and the major assemblies installed in the system. In September the conversion optics arrived from the vendors for local testing and installation. Beamline alignment was completed in September, and we began to tune the assembled conversion cells. At present we plan to fire 12 UV beams on target by 22 October.

Other activities during this quarter included the work on the x-ray probe beam project, and the active-mode-locked, Q-switched oscillator project scheduled for late fall implementation in both OMEGA and GDL.

A summary of OMEGA operations this quarter follows:

Target Shots	50
Beamline Test Shots	0
Driver Test Shots	17
Software Test Shots	13
TOTAL	80

A summary of OMEGA operations for FY84 follows:

Target Shots	618
Beamline Test Shots	221
Driver Test Shots	292
Software Test Shots	207
TOTAL	1338

ACKNOWLEDGMENT

This work was supported by the U.S. Department of Energy Office of Inertial Fusion under contract number DE-AC08-80DP40124 and by the Laser Fusion Feasibility Project at the Laboratory for Laser Energetics which has the following sponsors: Empire State Electric Energy Research Corporation, General Electric Company, New York State Energy Research and Development Authority, Northeast Utilities Service Company, Ontario Hydro, Southern California Edison Company, The Standard Oil Company, and University of Rochester. Such support does not imply endorsement of the content by any of the above parties.

1.C A New Front-End Design for OMEGA

We have recently completed the design of a new front end for the OMEGA laser system and are now constructing a full-scale prototype. The purpose of this project is to implement fully active mode-locked and Q-switched (AMQ) oscillators[1] in OMEGA and to improve control of the beam profile. The new front end is commonly referred to as the predriver, because it is a subsystem to replace all the present components between the oscillator and the first driver-line amplifier. Three important design requirements for the predriver are high-contrast pulse switchout, pulse amplification, and readily adjustable beam profile.

The optical design is based on both measurements and computations. Over the past five years we have made many measurements of the oscillator output profile and the beamline output profile and energy, and have compared the measurements with optical ray-trace code predictions in order to calibrate the code. Agreement of the measurements and *RAINBOW* code predictions has improved steadily and is now extremely close as shown in Fig. 20.1. As a result, we are confident that we can characterize the AMQ oscillator output experimentally and use these data as input to *RAINBOW* for predriver design evaluation.

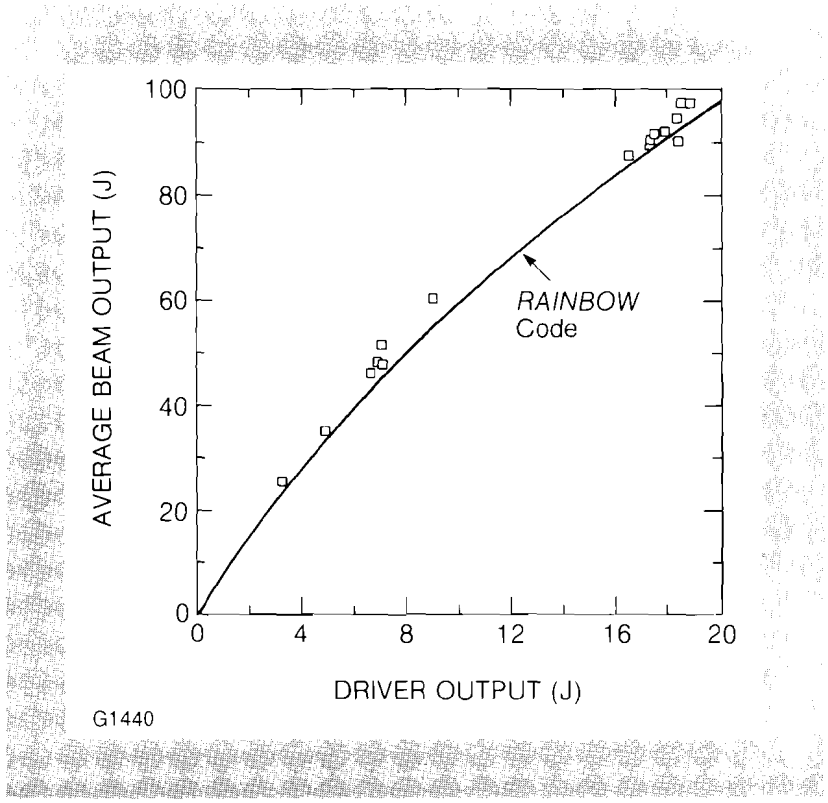

Fig. 20.1
Comparison of the predicted and observed OMEGA beamline output characteristics for 1.0-ns FWHM pulse duration.

The prototype under construction will be used to debug the pre-driver configuration and to identify and eliminate reliability problems. Experience with the prototype will also be helpful in developing new operation and maintenance procedures.

Motivation for New Design

The active/passive mode-locked, Q-switched OMEGA oscillators are reliable, high-energy output devices (1 mJ per pulse at 1 ns). However, it is inconvenient to change the pulse duration of an active/passive oscillator and virtually impossible to synchronize two of them. That is why we decided to convert to fully active oscillators.

Previous AMQ oscillators have been operated successfully with both YAG and YLF as lasing media. The lasing wavelength of YAG, at 1.064 μm, is too far from OMEGA's phosphate-glass wavelength of 1.054 μm, but YLF (1.053 μm) is well matched. Unfortunately, the optical quality of YLF was limited by existing materials technology, so we chose to use Q-100 phosphate glass[2] as the oscillator lasing medium. With Q-100 as the active medium, the oscillator output is optically clean, but the measured single-pulse energy is only 25-50 μJ. This is less than one-tenth the output of active/passive oscillators at 1 ns and requires a compensating gain of 20 - 40.

In the existing driver line, there is no reserve gain. A 1-ns oscillator pulse of 1-mJ energy is amplified to a maximum driver output of 20 J. At this driver output level, OMEGA attains a total 24-beam output of slightly more than 3 kJ. Although that output level is consistent with damage limits on present optical coatings, new damage-resistant

coatings are now available. If a few key elements were recoated, then the system could be operated safely at an output of 4 kJ, but only if the driver output could be increased to more than 30 J.

These two factors — lower oscillator output and greater required driver output — establish the predriver gain specification. Including some reserve, the predriver gain should be 30-50.

Increasing emphasis on target illumination uniformity and the installation of frequency-tripling crystals at the beamline outputs make it necessary to control the beams' phase and amplitude distributions very closely. Preferably, control is carried out early in the chain, as near as possible to the oscillator output. With the present front-end configuration shown in Fig. 20.2, this is a tedious process. The adjustable parameters are the focal length and location of the single collimating lens and the diameters of the hard aperture and the pinhole in the air spatial filter (ASF).

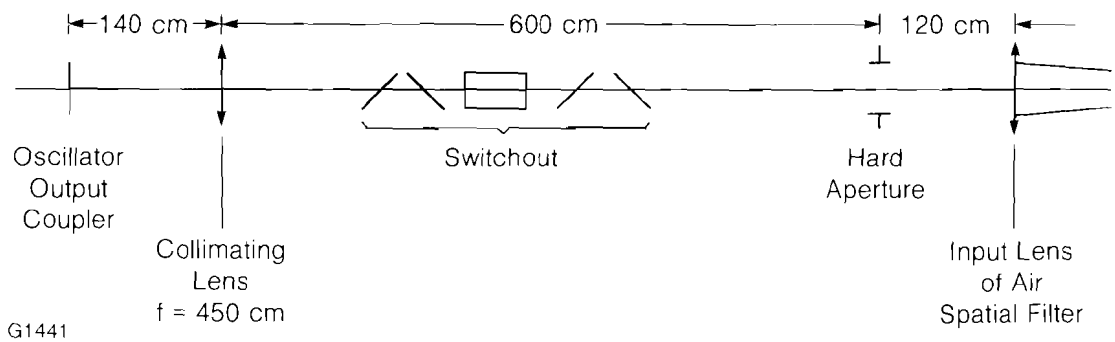

Fig. 20.2
Schematic diagram of the optical arrangement of the present OMEGA front end.

Changes made to the oscillator configuration itself usually require that all four of these parameters be adjusted. The adjustments are interactive, and their effects take some time to confirm quantitatively. One or more driver amplifiers have to be fired to obtain beam photographs, and then the photographs have to be processed and analyzed.

Another requirement for the new predriver, therefore, is that simple and effective adjustments be provided for beam phase, intensity profile, and fill factor.

Contrast between the pulse and baseline noise is excellent in the existing configuration. Three carefully timed Pockels cell/polarizer assemblies are fired by a low-jitter, laser-triggered silicon switch to provide a contrast ratio of $> 10^9$. This contrast should be maintained in the new predriver.

Basic Staging

The basic staging of the new OMEGA predriver is shown in Fig. 20.3. The major changes from the old configuration are the addition of a new preamplifier, the insertion of two new relays, and the addition of a zoom-lens assembly at the output of the ASF.

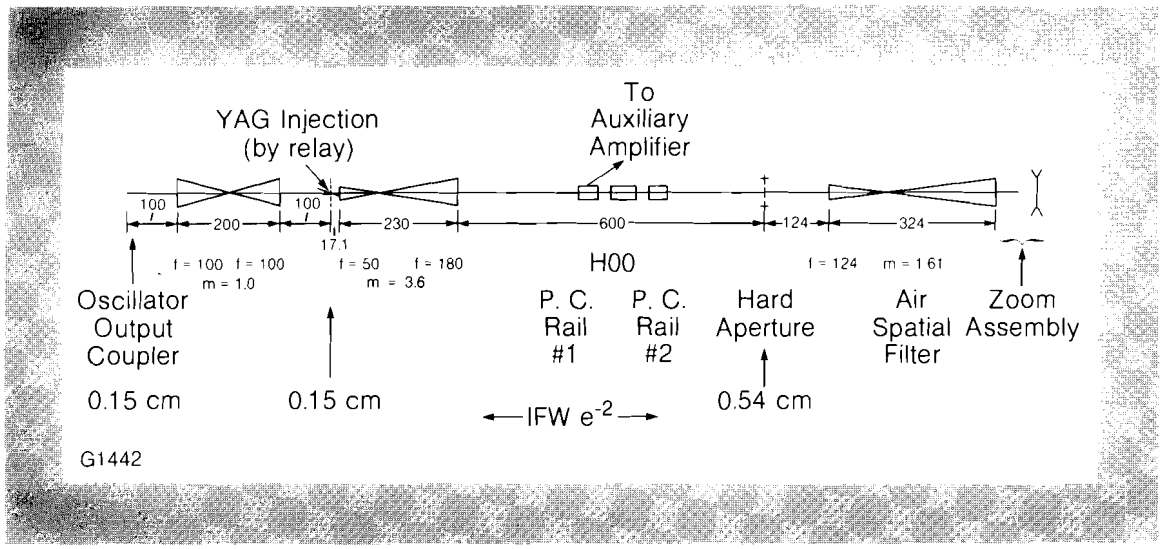

Fig. 20.3
Schematic diagram of the optical arrangement of the new front end for OMEGA.

For the new preamplifier, we chose a 16-mm-diameter head. This head is identical with the first head in the current OMEGA driver line and has a net small-signal gain (center line) of 100. This is three times the additional gain needed at 1 ns. The e^{-2} full-width intensity of the beam in the rod is approximately 4.4 mm; at this diameter, the beam will not be reshaped appreciably by the radial gain variation in the amplifier. Maximum repetition rate of this head is one shot per minute.

The output-coupling mirror of the AMQ oscillator has been fixed as a flat reflector. For oscillator pinholes that are not too small,[3] this assures a Gaussian-beam waist there. This flat phase front is then relayed to the hard aperture plane. We chose to do this with two separate relays, rather than a single relay. This option allows ample space for a mirror pair for oscillator pointing and a kinematic mirror, if desired, for rapid changeover to a second AMQ oscillator. In addition, a real image of the oscillator output coupler is formed at a convenient location for alignment laser injection and near-field diagnostic photography. The image plane of the first relay is located inside the front focal plane of the magnifying relay and the output image of the magnifier is 6 m from the output lens. The switchout is located at this magnified image point. Since the entire region up to the hard aperture is governed by Gaussian-beam propagation, there are no pinholes in either of the first two relays.

Finally, with this relayed system, future oscillators may replace the AMQ oscillators in a straightforward manner. All that is required is that they have flat output mirrors. A minor change in the spot size is accommodated by adjusting the zoom lens; a greater change, by altering the magnification of the second relay. A Gaussian profile is not required at the output coupler, but a flat phase front is desirable.

Control of the Beam Profile

Compensation for the substantial radial-gain variation in OMEGA requires close control of the transverse beam profile. Figure 20.4 is a plot of the calculated small-signal gain relative to the center-line gain of the entire system normalized to the clear aperture of the final

amplifier (note that the gain scale is logarithmic). In order to find the input profile that maximizes the fill factor of the final amplifier, it is necessary to use the ray-trace code, *RAINBOW*. *RAINBOW* uses measured radial gains for each amplifier in the chain and radial birefringent losses in a Frantz-Nodvik model to predict OMEGA's output. *RAINBOW* is applied to the relayed portion of the system beginning with the output of the zoom-lens assembly.

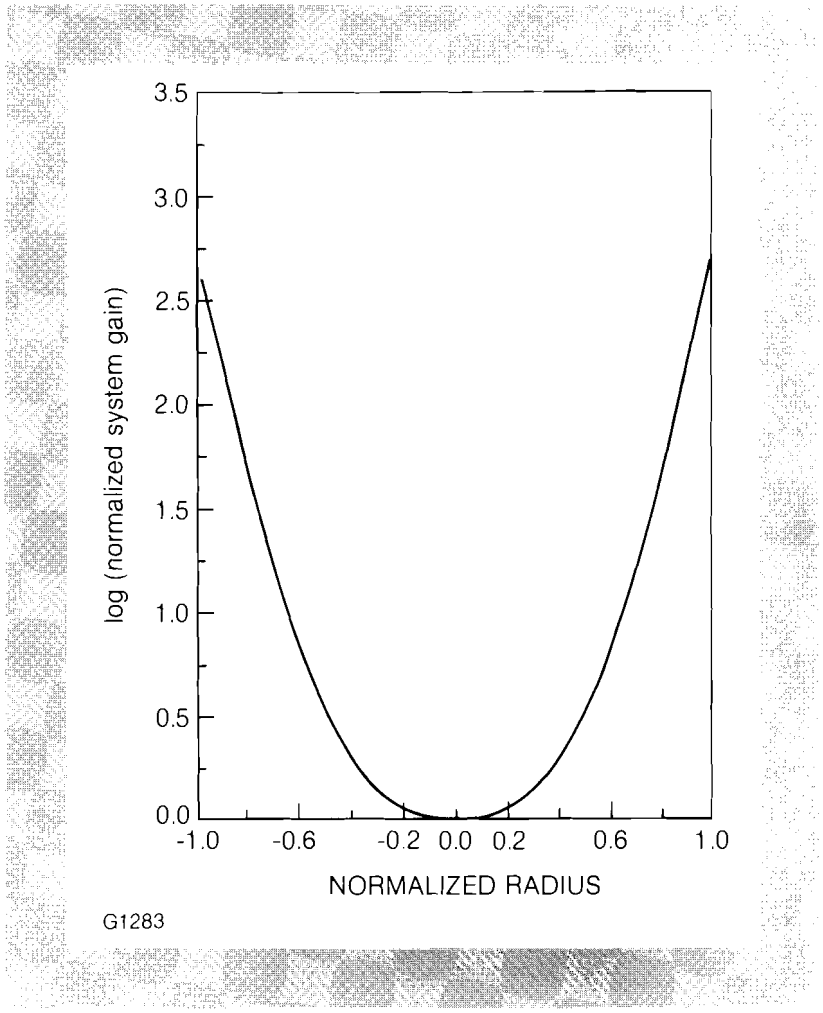

Fig. 20.4
Small-signal gain profile for the entire OMEGA amplifier chain, normalized with respect to centerline gain and clear aperture of the final amplifier.

We know from simulations and from experience that the starting intensity profile is required to have a value of zero at and beyond some finite radius and that it be smoothly convex inside. The shape should be approximately quadratic. A straightforward method for generating such a profile is to clip a Gaussian-profile beam on a hard aperture, propagate the beam through a spatial filter, and clip it again at its diffraction minimum with a second aperture. A simple diffraction code was written to model this process. The output of this code was used to initiate *RAINBOW*.

Three independent parameters are available for beam-profile adjustment. The first is the ratio of Gaussian-beam radius ω_0 to hard-aperture radius A. The second is the cutoff frequency of the ASF, and the last is the zoom-lens magnification. If the ratio ω_0/A is infinite, an

Airy pattern is produced at the ASF pinhole. One finds that the pattern there is still very similar to an Airy pattern for ω_0/A ratios as low as 0.6. This corresponds to clipping the profile at an intensity level equal to 0.004 times the on-axis intensity.

Figure 20.5 shows the change of beam profile in the ASF image plane with ASF pinhole size for infinite ω_0/A. When the radius of the pinhole is equal to the radius of the first Airy zero, the ASF image amplitude profile coincides with curve A of Fig. 20.5. If the radius of the pinhole is extended to equal the radius of the second Airy zero, the image amplitude profile peaks at a nonzero radius and passes through zero closer to the axis (curve B). This happens because the light between the first and second zeros of the Airy pattern is of opposite phase from the light in the central disk and subtracts from the central image amplitude. How much is subtracted depends upon the ASF pinhole diameter. By adjusting the pinhole diameter, the amplitude distribution may be varied continuously between the two profiles drawn in Fig. 20.5.

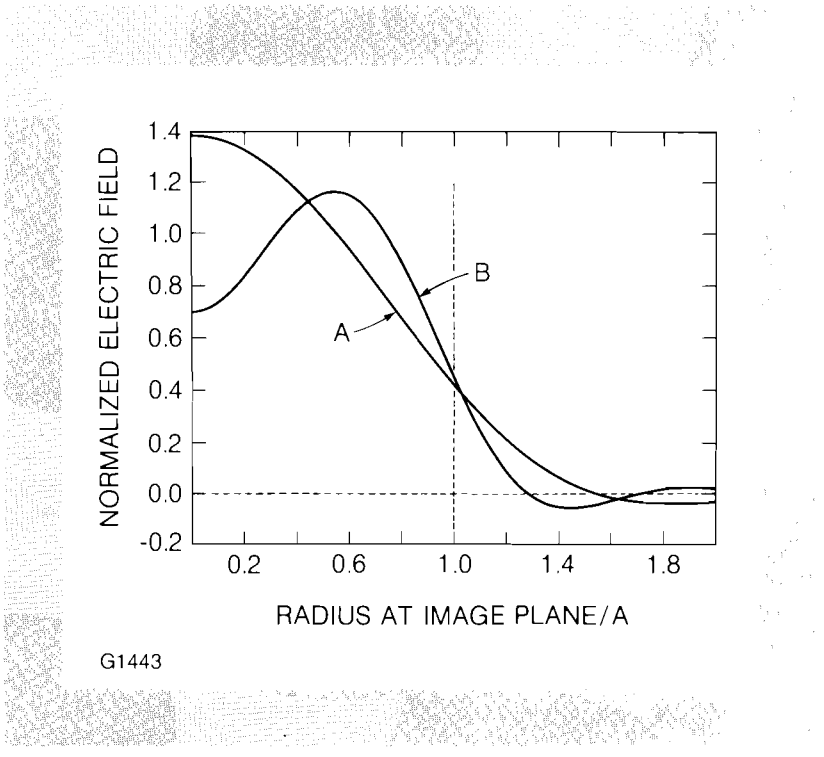

Fig. 20.5
Amplitude of the electric field in the image plane of the air spatial filter:
Curve A: for air-spatial-filter pinhole radius = first Airy zero radius.
Curve B: for air-spatial-filter pinhole radius = second Airy zero radius.

Qualitatively, the result is the same for finite ω_0/A ratios. The principle effect of changing ω_0/A is to change the amount of light in the second Airy ring which slightly alters the range of available amplitude profile shapes.

To avoid propagating the additional rings that appear in the image plane outside the first zero, the rings are clipped by a "scraper" aperture after the ASF. This effectively eliminates the peripheral ring structure from the beam profile. Any rings produced by subsequent spatial filtering have a calculated intensity less than 10^{-5} times the peak intensity.

Modeling the beam propagation has led to a suggested procedure for adjusting the beam profile. First, the ratio ω_0/A is set for an acceptable range of image modulation. Precision is not critical; a ratio of 0.9–1.0 is a reasonable choice. Next, the ASF pinhole size is chosen to produce an appropriate driver input profile. Finally, the zoom-lens magnification and scraper aperture are set. The most difficult case to handle is long-pulse operation because of gain saturation. The predicted output of OMEGA at 1 ns for intermediate drive is shown in Fig. 20.6. For this worst case the system can operate over a range of profiles from nearly flat to reverse quadratic.

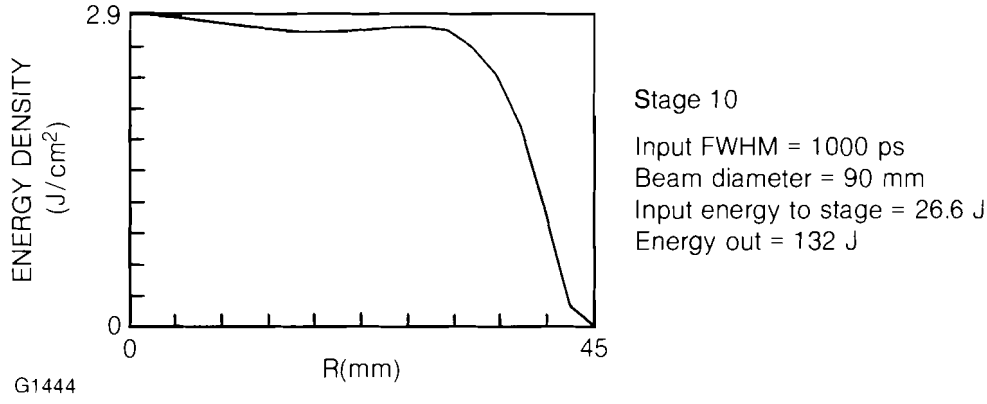

Fig. 20.6
Predicted OMEGA output profile for intermediate drive.

Schedule

When the front-end prototype is completed, measurements of its beam profile will be compared to the profile of the current driver-line input and to the profile expected on the basis of modeling. Energy output and the contrast and transmission of the pulse switchout will also be characterized. Installation on OMEGA is scheduled to begin in December.

ACKNOWLEDGMENT

This work was supported by the U.S. Department of Energy Office of Inertial Fusion under contract number DE-AC08-80DP40124 and by the Laser Fusion Feasibility Project at the Laboratory for Laser Energetics which has the following sponsors: Empire State Electric Energy Research Corporation, General Electric Company, New York State Energy Research and Development Authority, Northeast Utilities Service Company, Ontario Hydro, Southern California Edison Company, The Standard Oil Company, and University of Rochester. Such support does not imply endorsement of the content by any of the above parties.

REFERENCES

1. G. Albrecht, M. Gruneisen, and D. Smith, Technical Digest of the Conference on Lasers and Electro-Optics (Optical Society of America, Washington, D.C., 1983), Paper TuM10. Submitted to *IEEE J. Quantum Electron.*
2. Product of Kigre, Inc., Toledo, OH.
3. H. P. Kortz and H. Weber, *Appl. Opt.* **20**, 1936 (1981).

Section 2
PROGRESS IN LASER FUSION

2.A Irradiation Uniformity Measurements for Six UV (351-nm) OMEGA Beams

The success of direct-drive laser fusion requires detailed knowledge and control of the illumination uniformity on a spherical target irradiated with multiple beams. Studies of this issue have been a principle part of the laser-fusion program at LLE for some time.[1-3] For 24-beam experiments with 1-ns, 1053-nm IR pulses, we have used the measured intensity distribution of the beams in the equivalent target plane (ETP) to simulate the actual target irradiation uniformity.[4] We estimate the uniformity in a similar fashion for six-beam UV illumination.

For the IR beams, we begin with ETP photographs recorded in the beam-diagnostic packages (BDP's) installed in each OMEGA beam.[5] The photographs are scanned, digitized, and intensity corrected, and an azimuthally averaged intensity profile is obtained for each beam. These profiles are inserted into a spherical beam-superposition code[3] which maps the intensity profiles onto the surface of a spherical target for specific beam geometries and focusing conditions. This superposition code also models refraction of the laser-light rays in the corona of the laser plasma and includes simplified descriptions for the laser-plasma absorption. The result is an overall estimate of the energy deposition uniformity which can be used to estimate the target-drive nonuniformity in two-dimensional (2-D) simulations of laser-fusion-target implosions.

With the conversion of the output of OMEGA from IR to UV (351 nm),[6] the assessment of the irradiation uniformity presents new problems. The nonlinear intensity dependence of the frequency conversion process[7] tends to accentuate spatial variations in the intensity profiles of the beams propagating through the conversion crystals. In addition, the crystals and following optics in the beamline can introduce phase modulation into the beam which is subsequently transformed into intensity modulation in the target plane.

Concurrent with the activation of the first six UV beams of OMEGA during the fall of 1983, an experimental program was established to measure the 2-D intensity distribution of each beam in the target plane.[8] The optical system for obtaining both IR and UV ETP photos of each of the up-converted beams of OMEGA has been described previously.[9] The energy in each beam is measured with a multiwavelength energy-sensing system (MESS) comprised of a 20-cm aperture calorimeter and three photodiodes in conjunction with an integrating sphere.[10]

Figure 20.7 shows individual images of the ETP intensity distribution for three of the up-converted beams in both the IR and UV, recorded at an equivalent target plane located 1,600 μm inside best focus. The IR-beam image shows a clear ring structure. This structure is replicated in the UV distribution. Improvement in the front-end driver-line optics of OMEGA to be made in the fall of 1984 should markedly improve these distributions.

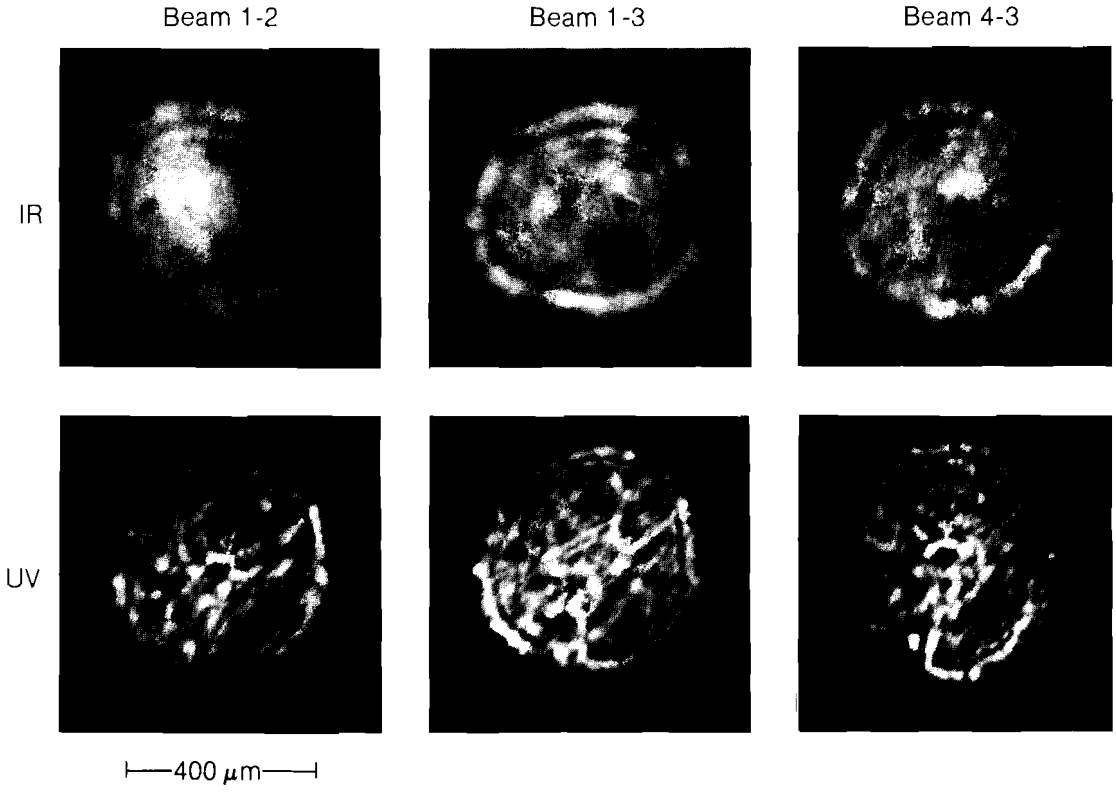

Fig. 20.7
Characteristic intensity distributions in the target plane for three of the six unconverted OMEGA beams. Shown are the IR and UV intensity distributions for tangential focus on the surface of a 400-μm-diameter spherical target. With the current beam output, the mean UV intensity on the surface of the target would be $\sim 5\times10^{13}$ *W/cm*^{2}.

The ETP images are digitized on a Perkin-Elmer PDS microdensitometer, with the known intensity ratio of successive images to calibrate the film response. The resulting data array describes the image intensity as a function of position in the ETP.

Figure 20.8 shows the iso-intensity contours (12% contour intervals) of the six UV beams. These particular records were obtained for the same ETP located 1,600 μm inside best focus. They correspond to the intensity distributions in each beam on the surface of a spherical, 215-μm-radius target when each focus lens is adjusted to focus the beam eight target radii beyond the center of the target.

An overall assessment of the illumination uniformity achieved on a spherical target is made with a new spherical, 2-D, beam-superposition code.[11] This code maps the overall intensity distribution on a spherical target, utilizing the individual 2-D intensity distributions recorded for each beam with the correct beam orientation, beam geometry, and focusing conditions; azimuthal averaging is not applied to the beam profiles.

For composite six-beam distributions it is assumed that the total laser energy is divided approximately equally among all six beams.

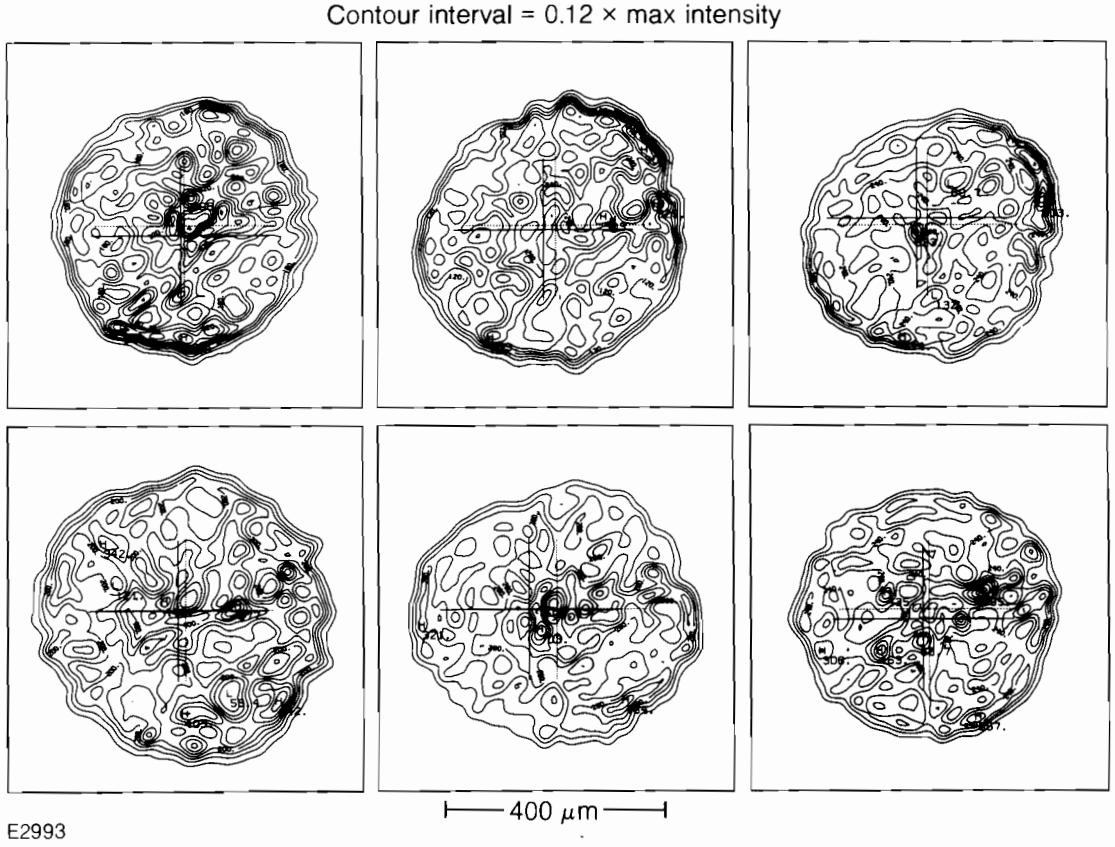

Fig. 20.8
Iso-intensity contour plots of the intensity distributions in all six UV beams at a distance of 1600 μm from best focus. This corresponds to the intensity distribution of each beam when focused for tangential overlap on a 400-μm-diameter target.

The actual minimum beam-to-beam energy variance in OMEGA depends upon the accuracy of the energy-measurement system. Precise reapportionment of the beam-output energies is currently limited by the MESS-diode calibration variance. This is due, in turn, to residual electrical and thermal noise in the signal from the thermoelectric calorimeters used to calibrate the diodes. With the present calorimeter-calibration uncertainty, it is possible to balance the on-target energies of the six UV beams to $\approx$ 3% rms, so the assumption of equal beam energies is valid.

In order to assess nonuniformity quantitatively for specific beam-focusing conditions, the corresponding surface intensity distributions are decomposed into spherical-harmonic modes.[3] The amplitudes of the low-order ℓ-modes are significant in determining the reaction of imploding laser-fusion targets to irradiation nonuniformities. Low-order ℓ-modes correspond to large-scale irregularities which will tend to be accentuated as the target implodes. Higher-order ($\ell > 20$) modes are not expected to affect the implosion greatly, since they correspond to small-scale fluctuations that will be reduced by thermal smoothing.

Shown in Fig. 20.9 are the amplitudes of the first 11 ℓ-modes for three different focusing conditions with six UV beams on target. The level of nonuniformity, taken as the quadrature sum of the first 11 ℓ-mode amplitudes, decreases as expected when the focus parameter is increased from 6 R through 8 R (tangential focus). If there were

Fig. 20.9
Decomposition of the intensity distribution shown in Fig. 20.8 in terms of the amplitudes of specific, low-order, spherical harmonic modes. The level of non-uniformity, as depicted by the amplitude of specific ℓ-modes, decreases as the beams are focused further beyond the target.

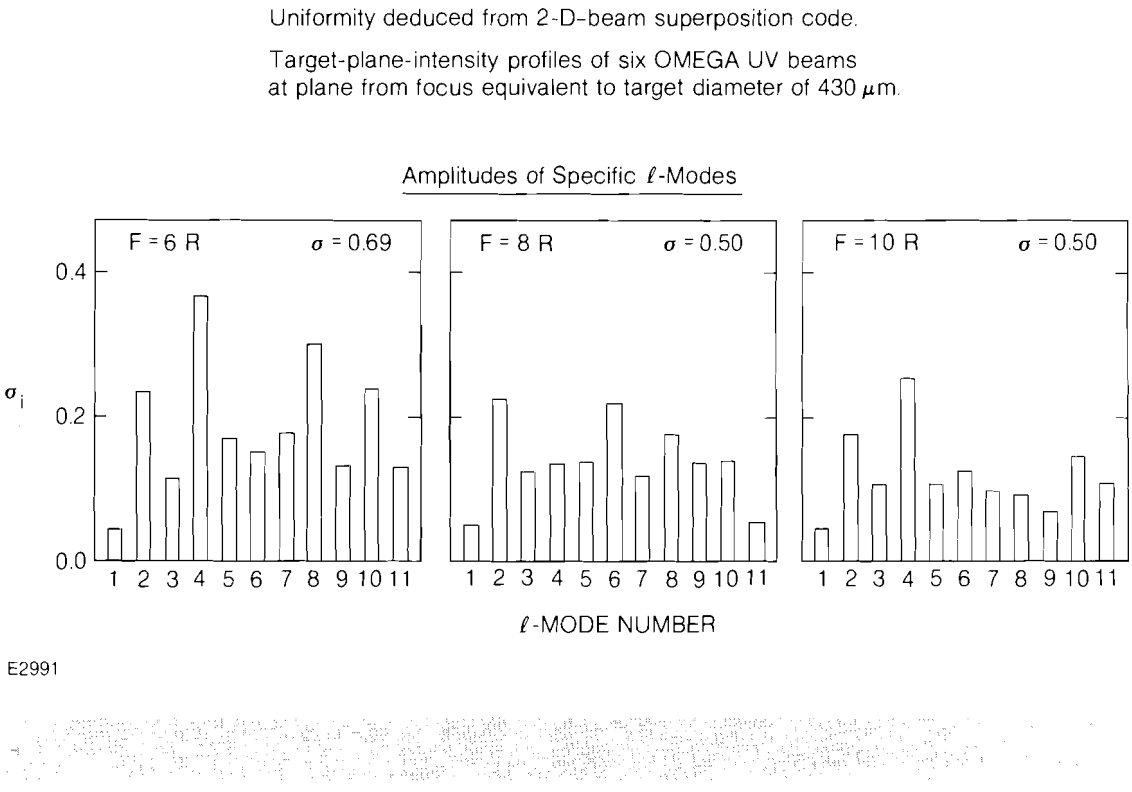

more than six beams, the nonuniformity at 10 R would be less than at 8 R. Here, the focus parameter is the number of target radii beyond the center of the target at which the geometric focus of the beam is located. The level of nonuniformity estimated for six IR beams for identical focus parameters is comparable.[12]

These nonuniformity estimates are base-line data for measuring future improvements in irradiation uniformity. Considerable improvement is expected as a result of converting all 24 beams to the UV. In addition, we are working to improve our control of the intensity distribution in each beam and to reduce the beam-to-beam energy imbalance.

ACKNOWLEDGMENT

This work was supported by the U.S. Department of Energy Office of Inertial Fusion under contract number DE-AC08-80DP40124 and by the Laser Fusion Feasibility Project at the Laboratory for Laser Energetics which has the following sponsors: Empire State Electric Energy Research Corporation, General Electric Company, New York State Energy Research and Development Authority, Northeast Utilities Service Company, Ontario Hydro, Southern California Edison Company, The Standard Oil Company, and University of Rochester. Such support does not imply endorsement of the content by any of the above parties.

REFERENCES

1. J. Hoose, R. Hopkins, S. Kumpan, J. Soures, J. Kelly, L. Iwan, J. Reynolds, and L. D. Lund, "Phase and Intensity Characteristics of the OMEGA High Power Glass Laser," *Proceedings of the Second Conference on Lasers and Electro-Optics (CLEO)*, Phoenix, AZ (1982).

2. M. C. Richardson, T. Boehly, R. S. Craxton, J. Delettrez, G. D. Enright, A. Entenberg, R. Epstein, W. Friedman, J. Hoose, R. Hutchison, S. Kacenjar, K. Lee, S. Letzring, R. S. Marjoribanks, R. L. McCrory, J. Rizzo, W. Seka, R. Short, S. Skupsky, J. M. Soures, C. Verdon, D. Villenueve, E. A. Williams, and B. Yaakobi, *Plasma Physics and Controlled Nuclear Fusion Research 1982*, Vol. 1, 477 (1983).

3. S. Skupsky and K. Lee, *J. Appl. Phys.* **54**, 3662 (1983).

4. M. C. Richardson, S. Skupsky, J. Kelly, L. Iwan, R. Hutchison, R. Peck, R. L. McCrory, and J. M. Soures, "Laser Fusion Target Irradiation Uniformity with the 24-beam OMEGA facility," *SPIE Vol. 380, Proceedings of the 1983 Los Alamos Conference on Optics*, 473 (1983).

5. J. Bunkenberg, J. Boles, D. C. Brown, J. Eastman, J. Hoose, R. Hopkins, L. Iwan, S. Jacobs, J. H. Kelly, S. Kumpan, S. Letzring, D. Lonobile, L. D. Lund, G. Mourou S. Refermat, W. Seka, J. M. Soures, and K. Walsh, *IEEE J. Quantum Electron.* **QE-17**, 1620 (1981).

6. J. M. Soures, R. J. Hutchison, S. D. Jacobs, L. D. Lund, R. L. McCrory, and M. C. Richardson, "OMEGA — A Short Wavelength Laser for Fusion Experiments," presented at 10th Annual Meeting of the American Nuclear Society, Philadelphia (1983).

7. R. S. Craxton, *Opt. Commun.* **34**, 474 (1980).

8. M. C. Richardson, S. Skupsky, J. M. Soures, W. Lampeter, S. Tomer, R. J. Hutchison, M. Dunn, and W. Beich, *Proc. CLEO '84*, paper FK3 (1984).
9. LLE Review **17**, 7 (1983).
10. L. Iwan, D. Quick, and W. Seka, *Proc. CLEO '84*, paper FK4 (1984).
11. S. Tomer, W. Lampeter, and M. C. Richardson (to be published).
12. M. C. Richardson, T. R. Boehly, B. A. Brinker, T. C. Bristow, R. S. Craxton, J. A. Delettrez, G. Enright, A. Entenberg, W. Friedman, L. M. Goldman, J. Hoose, R. J. Hutchison, L. Iwan, S. Kacenjar, K. Lee, S. A. Letzring, L. D. Lund, R. S. Marjoribanks, R. L. McCrory, J. M. Miller, J. Rizzo, W. D. Seka, S. Skupsky, J. M. Soures, C. P. Verdon, D. M. Villeneuve, E. A. Williams, and B. Yaakobi, *Laser Interaction and Related Plasma Phenomena*, Vol. 6, 903 (1984).

2.B Polymer Microballoon Development

For many years inertial-confinement-fusion (ICF) experiments have been conducted with DT-filled, glass microballoon targets. The attractive properties of glass shells are their low permeability to DT gas and relatively high tensile strength, which enables them to withstand fairly high internal pressures. However, the use of high-Z silica glass promotes radiative preheat of the fuel when illuminated by a UV laser. This reduces the maximum obtainable fuel compression. Low-Z polymer microballoons can minimize this effect and also provide uniform ablative surfaces. Moreover, experimental diagnosis of the fuel core is easier because low-Z polymers are more transparent to the soft x rays generated during the implosion. But for ICF target fabrication, the polymer microballoons must have mechanical properties comparable to those of glass, i.e., high tensile strength and low permeability.

Two methods of polymer shell fabrication are currently being investigated at major ICF laboratories. First, there is the drop or spray tower method in which a liquid-phase bubble is generated at the top of a vertical column and passed through a heated zone to drive off the solvent. The solid polymer shell is collected at the bottom of the tower in a water bath. The second technique is to microencapsulate water with a polymer solution and then drive off the solvent to produce a shell. This second method is the one we are pursuing here at LLE.

This particular microencapsulation technique was developed by Kubo[1] and is depicted in Fig. 20.10. The polymer is solvated in a low-boiling-point, high-vapor-pressure solvent that is normally immiscible or slightly soluble in water. Under continuous agitation a water phase containing approximately 50 ppm of surfactant is emulsified in the polymer solution. The resulting emulsion is a continuous polymer (*oil*)

phase with water droplets uniformly distributed throughout. After 20 min of agitation with a mechanical stirrer the droplet size is relatively uniform, with an average diameter that is a function of the speed of agitation. The emulsion is then poured into a second water phase containing approximately 600 ppm of surfactant. The result is a suspension in the second water phase of small polymer "bubbles" containing the first water phase. This solution is heated to drive off the polymer solvent, leaving polymer shells containing the first water phase. Finally, the shells are collected by sieving and gently heated to remove the interior water.

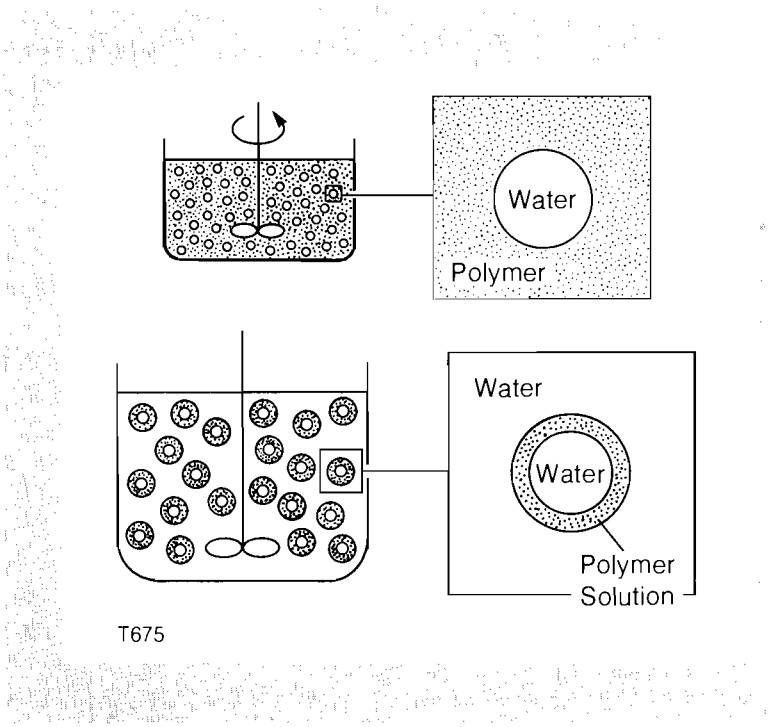

Fig. 20.10
The microencapsulation process for producing polymer-shell microballoons.

The focus of the University of Rochester's LLE microencapsulation program is on materials development rather than process development. Originally, Kubo's work was conducted with polystyrene (PS), a polymer which is easily solvated and exhibits favorable characteristics for microencapsulation. However, PS is a poor target material because of its relatively high permeability [23.3×10^{-10} cc hydrogen cm/(cm^2 • sec • cm Hg)] and low tensile strength (40-70 N/mm^2).[2] More suitable polymers include polyacrylonitrile (PAN), polyvinyl alcohol (PVA), and regenerated cellulose, all of which exhibit permeabilities that are five orders of magnitude lower than that of PS and tensile strengths that are ten times greater. To date, most of the polymer microballoon development work at LLE has focused on PAN because it is relatively easy to process and is highly resistant to water. PVA and cellulose are known to be hydrophilic and quickly deteriorate upon exposure to water.

Good solvents for PAN generally have high boiling points and low vapor pressure, except for nitromethane which is similar to water. However, solvating PAN in nitromethane is difficult, requiring the application of heat (greater than 80°C) and continuous agitation for three to

four hours. Even after this period not all the polymer is in solution, and micron-sized particles which affect the quality of the balloons are present. To resolve this, a PAN blend of 94% PAN and 6% methyl acrylate (provided by E. I. du Pont de Nemours & Co.) has been used. This reduces the processing temperature to 60°C and the blend is more easily solvated than pure PAN. The anticipated increase in permeability due to the use of the copolymer has not yet been determined but it is expected to be less than one order of magnitude—an acceptable increment.

We have performed experiments with a solvent system consisting of 85% nitromethane, 10% water, and 5% 2,2,2-trifluoroethanol. The polymer is pulverized in a laboratory blender to a 20-μm size and introduced to the solvent at room temperature. The solution is then heated to 70°C and slowly agitated for one to two hours in a closed system. The first water phase is heated to the same process temperature before addition, and the speed of agitation is increased to achieve the desired shell size. After the required agitation time, the emulsion is siphoned through a heated line into the second water phase which has also been heated to 70°C. Care must be taken to keep the process temperature and the temperature of all equipment coming in contact with the solution above 60°C, or the solution begins to gel and particles form. The pressure may be reduced somewhat, depending on the temperature of the system, to accelerate solvent removal. When most of the solvent has been driven off, the microballoons are collected and gently dried at 35-40°C for 48 to 72 hours.

Polyvinyl acetate (PVAc), although it has better physical properties than PS (tensile strength = 30-50 and permeability = 8.9×10^{-10}) is still not suitable for target material. However, PVAc is easily converted to PVA through a transesterification shown in Eq. 1. The conversion of PVAc to PVA has not yet been seriously addressed at LLE but will be in the future.

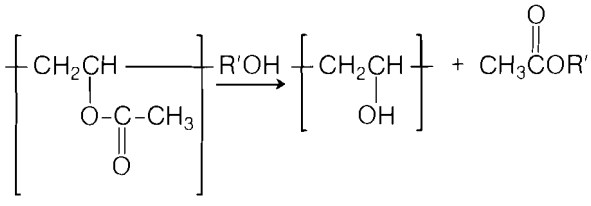

(1)

PVAc, like PS, is easily solvated by most solvents so that the process conditions are similar. The one notable exception is that the final suspension is cooled to 15-20°C to prevent coagulation as a result of heat softening of the polymer. (The softening point of PVAc is 28-31°C.)[3]

In experiments with PS, PAN, and PVAc, we have successfully produced target-quality balloons 50-400 μm in diameter, with wall thicknesses of 5-25 μm. Non-concentricity and sphericity are typically less than 5% (Fig. 20.11). The degree of success varies with the material. PS has been by far the most successful, with more than 50% yield of target-quality balloons. PAN, on the other hand, yielded only

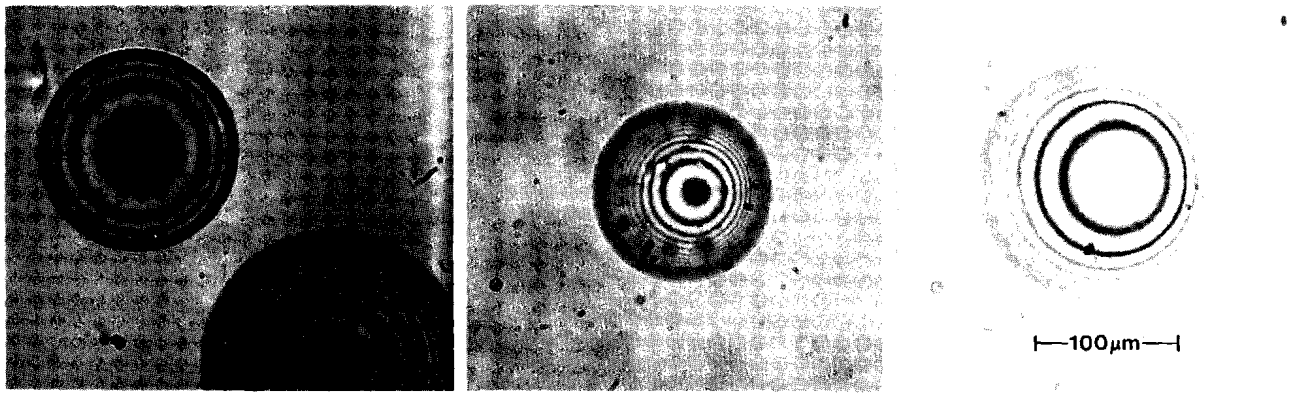

T697 (a) (b) (c)

Fig. 20.11
Interferograms of polymer microballoons manfactured using microencapsulation:
(a) polystyrene
(b) polyacrylonitrile copolymer
(c) polyvinyl acetate

10-20%; this is attributable to the lack of complete polymer solution. With respect to surface finish, both PS and PVAc microballoons exhibit surface roughnesses of less than 250 Å, but the presence of micron-sized particles degrades the surface finish of PAN microballoons (see Fig. 20.12).

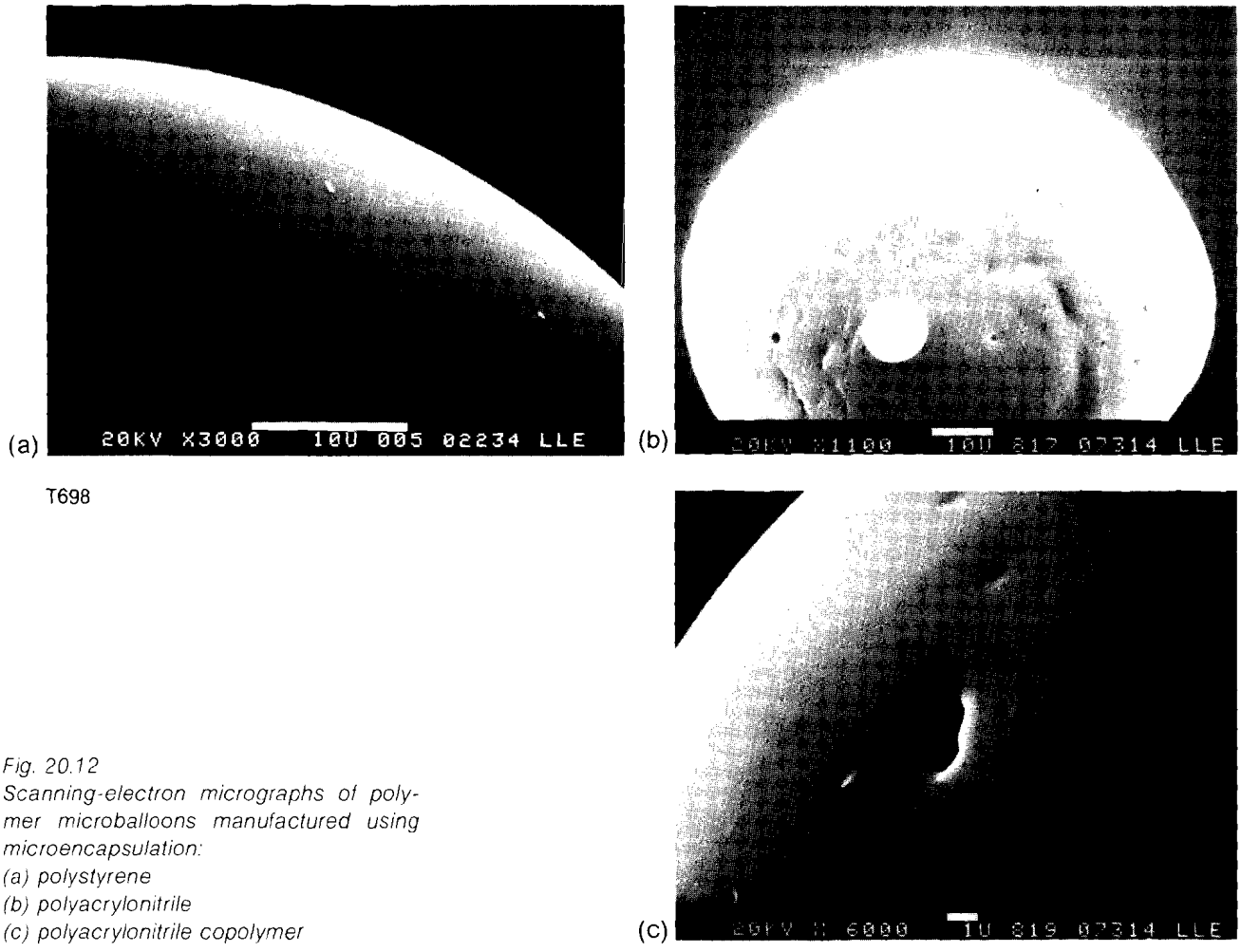

(a) (b) (c)

T698

Fig. 20.12
Scanning-electron micrographs of polymer microballoons manufactured using microencapsulation:
(a) polystyrene
(b) polyacrylonitrile
(c) polyacrylonitrile copolymer

Gentle removal of the interior water phase is very important if the microballoons are to survive. Overly vigorous drying tends to cause stress in the balloons and produces small surface cracks like those depicted in Fig. 20.13. This effect has been observed in microballoons with wall thicknesses less than 10 μm for removal temperatures greater than 50°C.

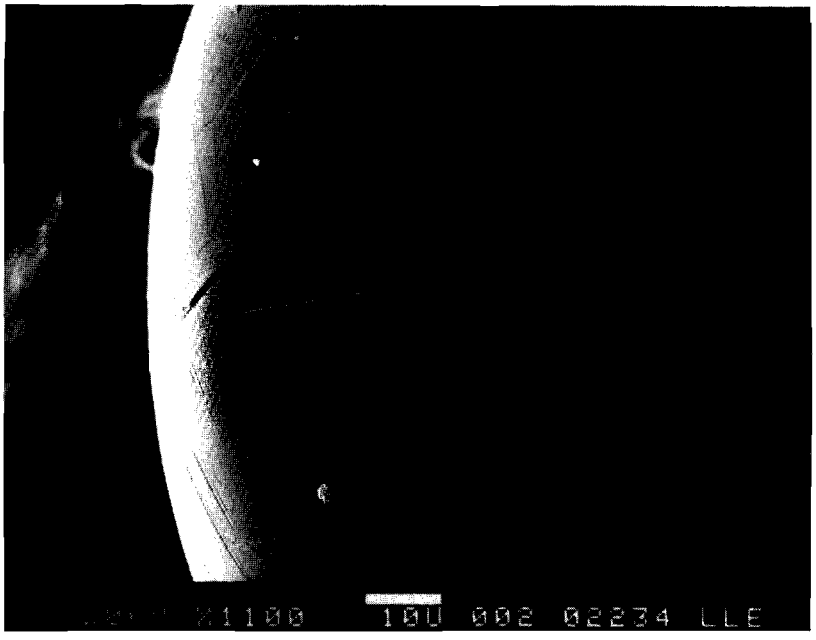

T699

Fig. 20.13
Scanning-electron micrograph of the surface of a polystyrene microballoon from which the interior water was removed too violently.

In short, we have employed microencapsulation techniques to fabricate target-quality microballoons with the polymers PS, PAN, and PVAc. To date, the highest yields and best surface finishes have been obtained with PS and PVAc. Although PAN microballoons are more difficult to produce, we continue to focus on this material because it is stronger and less permeable to hydrogen gas. We also plan to work further to explore the hydrolysis of PVAc to PVA.

ACKNOWLEDGMENT

This work was supported by the following sponsors of the Laser Fusion Feasibility Project at the Laboratory for Laser Energetics—Empire State Electric Energy Research Corporation, General Electric Company, New York State Energy Research and Development Authority, Northeast Utilities Service Company, Ontario Hydro, Southern California Edison Company, The Standard Oil Company, and University of Rochester. Such support does not imply endorsement of the content by any of the above parties.

REFERENCES

1. U. Kubo *et al.*, ILE Osaka University, ILE-APZ-79 (1979), p. 177.
2. *Polymer Handbook*, 2nd ed., edited by J. Branup and E. H. Immergut (Wiley, New York, 1974).

2.C Limits on the Flux Limiter and Preheat from Analysis of Implosion Experiments with 1054-nm Illumination

Thermal electron transport plays an important role in the performance of direct-drive inertial-confinement-fusion targets. The laser energy absorbed in the corona is carried into the dense target through thermal electron transport and is converted into kinetic energy through the ablation process. The efficiency of the target drive and of the absorption of the laser light depend to a large extent on the efficiency of the thermal transport. In laser-fusion hydrodynamic codes the thermal transport is calculated with a diffusion model using Spitzer's model for thermal conductivity.[1] In the steep temperature gradients which exist in laser-fusion targets, the diffusion model with Spitzer's conductivity yields thermal fluxes larger than those available from the free-streaming electrons.[2] Code calculations, therefore, usually impose an upper limit on the conductivity given by some fraction of the free-streaming value, with the form $Q_f = fnkT(kT/m)^{1/2}$ where the parameter f, known as the flux limiter, is to be determined through experiments or from solutions to the Boltzmann equation.

The early experimental determinations of the flux limiter have concentrated mainly on planar targets (see Ref. 3 for a survey of the literature on the subject) while more recent efforts have focused on spherical targets. From the analysis of planar transport experiments carried out at LLE with 351-nm illumination, one concludes that both the thermal transport and the absorption could be modeled with f = 0.04.[4] Spherical experiments with 1054-nm illumination at the Rutherford Laboratory[5] could be described by uninhibited transport ($f \gtrsim 0.1$). Similar experiments at LLE provided a more complex picture.[6] In these experiments the transport was obtained from the measurement of the burn-through of the heat front through a plastic layer to an aluminum or titanium layer and from the mass-ablation rate calculated from ion collector traces. Conclusions from this experiment are listed below.

(1) The burn-through to the aluminum substrate was a factor of 2 to 3 larger than predicted by the code.

(2) The burn-through to the titanium substrate was well modeled, using a flux-limited value f = 0.05; the absorption fraction was also calculated properly under this condition.

(3) The mass-ablation rate obtained from the charge collectors was lower than that obtained from burn-through measurements. Simulation of the ablation rate from the charge collectors required $f < 0.1$.

To explain these results it was assumed that the heat front was not as steep as is expected from code calculations, but that a 200- to 300-eV foot precedes the front in the high-density material. Such a

foot would explain the large burn-throughs to the aluminum substrate but would not contribute to the ablation process. It would be produced by hot electrons (several times the thermal velocity) streaming from the hot corona into the cold, dense matter.

In this article we present the results of simulating implosion experiments which are sensitive to the flux limiter and preheat. Unlike the transport experiments described above, the transport in the implosion experiments is not measured directly; it is inferred from conditions in the target at stagnation which are sensitive to the transport and preheat.

A detailed analysis was carried out for shot 7035. Although there were many other shots in the series, this particular shot was chosen because the x-ray microscope images show most clearly the double-ring structure characteristic of the targets in this regime. Also, the focusing at 10 radii behind the target resulted in one of the most uniform implosions.

In shot 7035 a glass microballoon of 400-μm diameter and 1-μm thickness, filled with a 20-atm equimolar mixture of DT, was irradiated by 2.11 TW of 1054-nm laser light for 1.02 ns. The peak nominal irradiance was 7.9×10^{14} W/cm^2. Focusing with f/4 optics at a distance of 10 radii beyond the target center provided a uniform surface-illumination pattern. The target absorbed 709 J (0.33 absorption fraction) and the neutron yield was 1.5×10^{8}.

Simulation Conditions

The simulations for the uniform implosion shots were carried out with the laser-fusion design code *LILAC*. *LILAC* is a 1-D, Lagrangian hydrodynamic code that includes ray tracing of the laser light in the computation of the absorption, radiation transport with a diffusion approximation using LTE opacity tables, transport of the suprathermal electrons created by resonant absorption, and a post-processor which generates microscope and streak images.

The 2-D ray tracing was carried out with the azimuthally averaged, experimental, laser-intensity profile obtained at the equivalent target plane; similarly, the experimental focusing-optics parameters, f-number and focusing distance, were included. At the turning point the fraction of the absorbed energy due to resonant absorption was estimated using a formula from Kruer.[7]

The calculated absorption fraction of 0.30 agrees with the experimental value of 0.33. About 16% of the absorbed energy is accounted for by resonant absorption (corresponding to 5% of the incident energy). An *r*-*t* plot of the implosion is shown in Fig. 20.14 with a superimposed plot of the laser pulse. The results discussed below were obtained with a "legislated" absorption option in order to perform the parameter study over the flux limiter and preheat under the same absorption conditions. In this option the deposition into the suprathermal electron component is adjusted to maintain the resonance-absorbed fraction at prescribed levels (16% and 32%), and any energy not absorbed by either the inverse-bremsstrahlung or resonant processes is deposited in the thermal component at the critical surface.

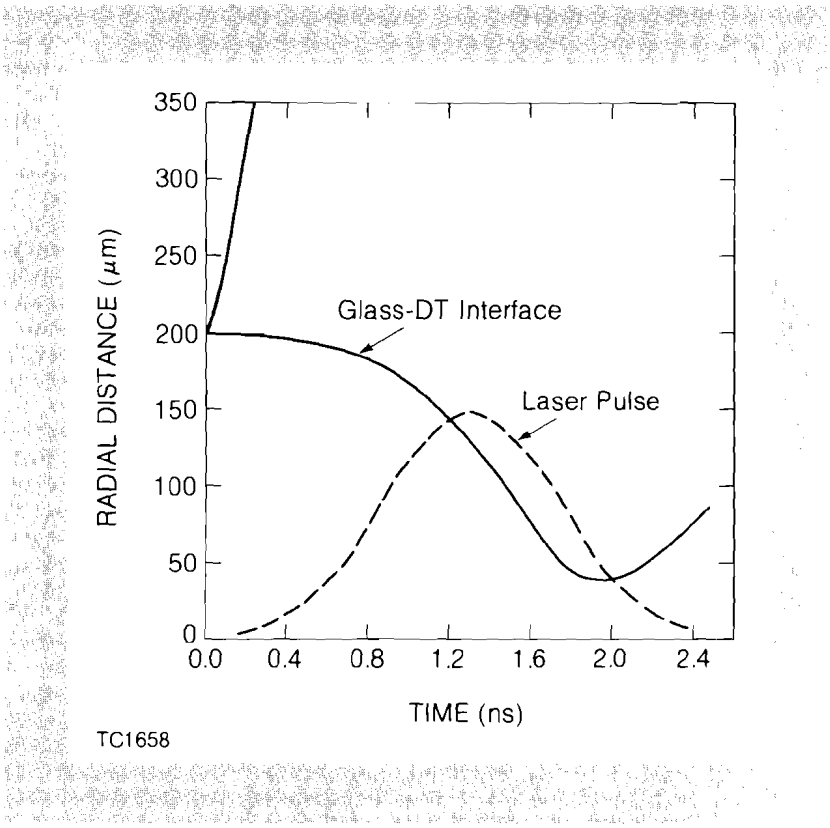

Fig. 20.14
Calculated trajectories of the outer surface of the target and of the glass-DT interface; the laser pulse is shown as a temporal reference.

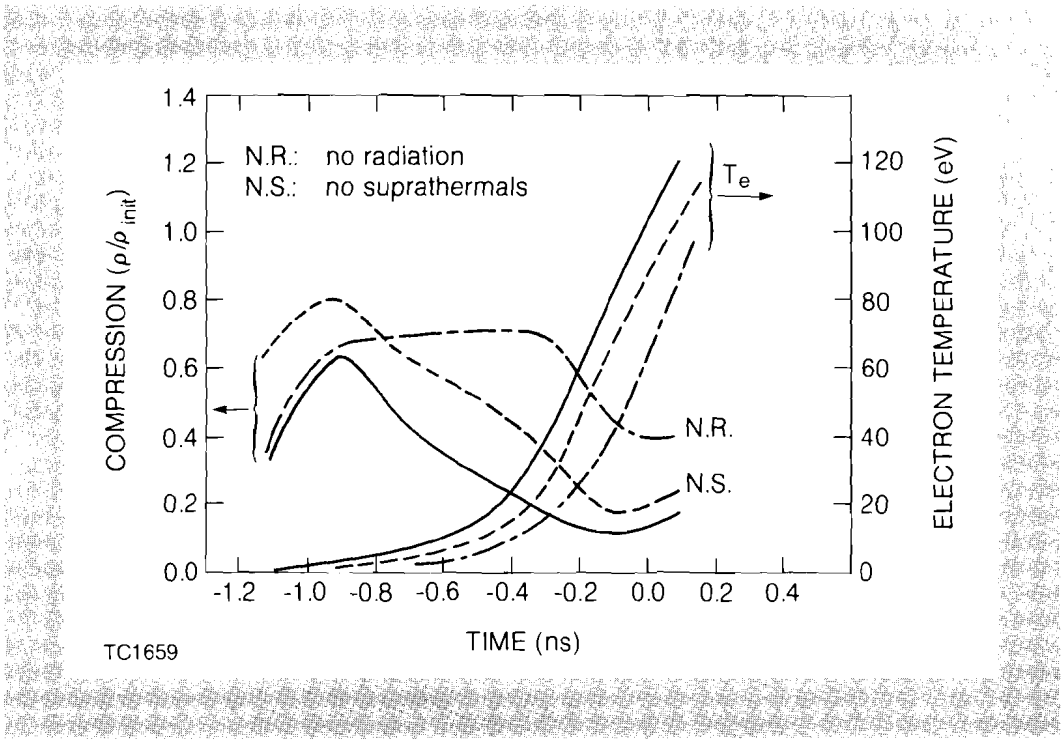

Fig. 20.15
Density and temperature in the pusher at a point initially 0.15 μm from the glass-DT interface during the implosion. Conditions were also calculated for no radiation and no suprathermals and are plotted for reference.

The dynamics of the implosion are those of an ablatively driven, "puffed-up" pusher. About 1 ns before the peak of the pulse, the glass shell is decompressed to ~ 0.2-0.3 times solid density by preheat from the initial shock, suprathermal electrons, and x-ray radiation. Figure 20.15 shows the conditions in the pusher during the implosion before recompression, for a position initially 0.15 μm inside the glass-DT interface. Most of the preheat in the first nanosecond is provided by the suprathermal electrons and the x-ray radiation from the hot plasma near the critical surface and in the heat front; each mechanism contributes about equally to the initial preheat. As the implosion proceeds, the radiation acts as a continuous preheat source which causes the shell to decompress to about 0.1 times solid density. The suprathermal electrons contribute little to the preheat during that time, so suppressing them from the computation hardly affects the conditions in the pusher. Suppressing the x-ray preheat has a much greater effect. The effect of the suprathermal electrons on the final implosion conditions and on the microscope images will be discussed later.

That the pusher is ablatively driven can be seen from the existence of an ablation front which progresses through the pusher. Figure 20.16 shows the electron temperature, mass density, and pressure profile in the pusher at one time during the implosion, 500 ps before the peak of the pulse. A typical ablation front has been set up with the pressure

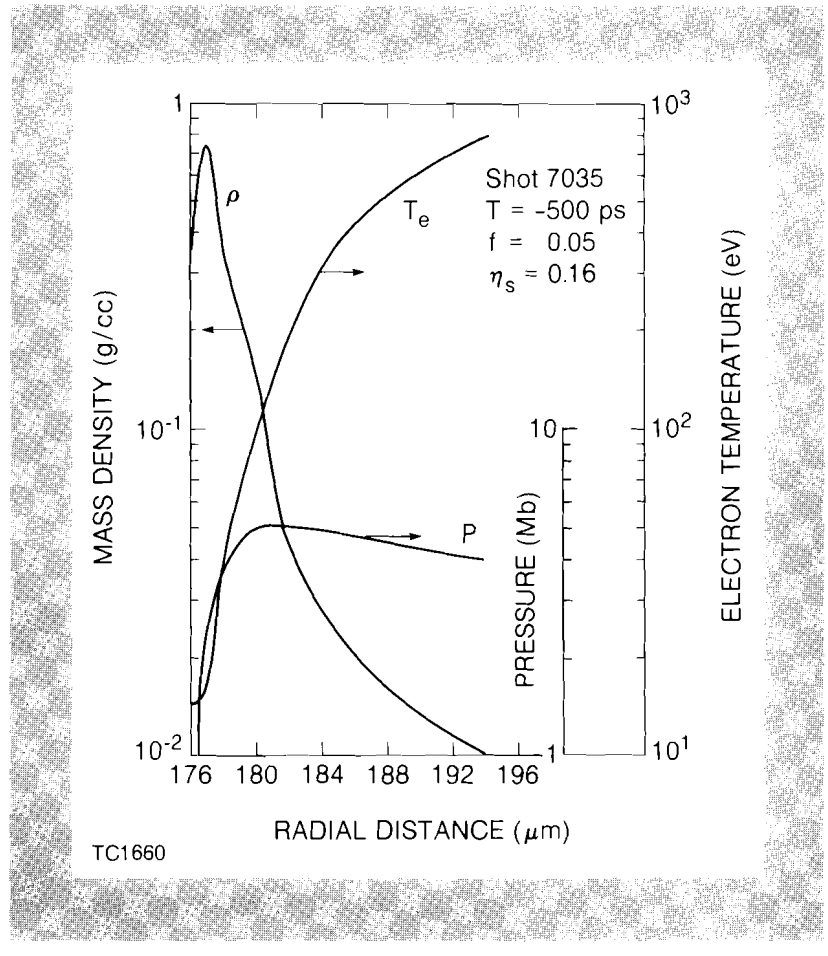

Fig. 20.16
Temperature, pressure, and density in the ablation region 500 ps before the peak of the pulse.

peak situated between the density and the temperature maxima. Other characteristics of the implosion, such as the progression of the ablation front through the pusher and the continuous ablation of target mass, indicate that the target is driven ablatively rather than explosively.

As the implosion proceeds, the pusher creates a shock wave in the fuel which preheats the fuel; this preheat is less than that in exploding pusher implosions because the pusher velocity increases more gradually. The pusher reaches a peak velocity of 2.4×10^7 cm/s. The shock wave reaches the center of the target about 90 ps after the peak of the pulse. The shock convergence and reflection raise the ion temperature in the central part of the fuel to several kilovolts and cause a neutron "burst" which lasts about 5 ps and produces about 1.2×10^9 neutrons. After shock reflection the pusher compresses the fuel to a peak density of 0.8 g/cc (four times that of liquid DT) with ion temperatures ranging from 0.4 keV near the pusher wall to 1.6 keV in the center. The compression phase produces another neutron burst of roughly the same magnitude as the previous one; the total neutron yield is 2.2×10^9 and the neutron-averaged ρR attains a maximum of 0.001 g/cm.

The experimental neutron yield was 1.8×10^8. A double burst of neutrons like that in the code simulation has been observed indirectly in measurements of the proton spectrum with a time-of-flight spectrometer by a group from the University of Illinois in similar experiments on the OMEGA laser system.[8] Both the measurements and the simulation with *LILAC* show a double-peaked proton spectrum which can be related to a double-peaked neutron production. A double-peaked proton spectrum is produced when conditions in the tamper, where the protons are primarily slowed down, are different for each neutron burst. Therefore, although the neutron yield of the simulation exceeds the experimental yield by about a factor of 10, not all the yield can be attributed to shock heating; a fraction of the experimental yield results from compression of the fuel by the glass pusher after shock reflection. Such compression heating requires reasonably good pusher symmetry during the implosion and stagnation. The lower experimental neutron yield is probably the result of lower temperatures during shock convergence because of imperfect spherical conditions. Such conditions may be due to non-uniformity in illumination and to the presence of the stalk. Lower shock-heating temperatures in the fuel lead to lower compression heating and, therefore, to a lower neutron yield.

The experimental x-ray microscope image and a scan of the film density along one diameter are shown in Fig. 20.17(a). The image shows a distinct bright outer ring surrounding a weaker ring and an inner structure which can be loosely interpreted as a bright inner ring. That weak/strong ring structure can also be observed in the scan. It also appears for two other combinations of filters. The microscope image obtained from the simulation is shown in Fig. 20.17(b) as a plot of the radial variation of x-ray intensity. The inner ring results from the x rays emitted from the inner surface of the glass pusher at stagnation. That surface is heated mostly by conduction from the DT fill and by the reflected shock. The outer ring is produced by the almost

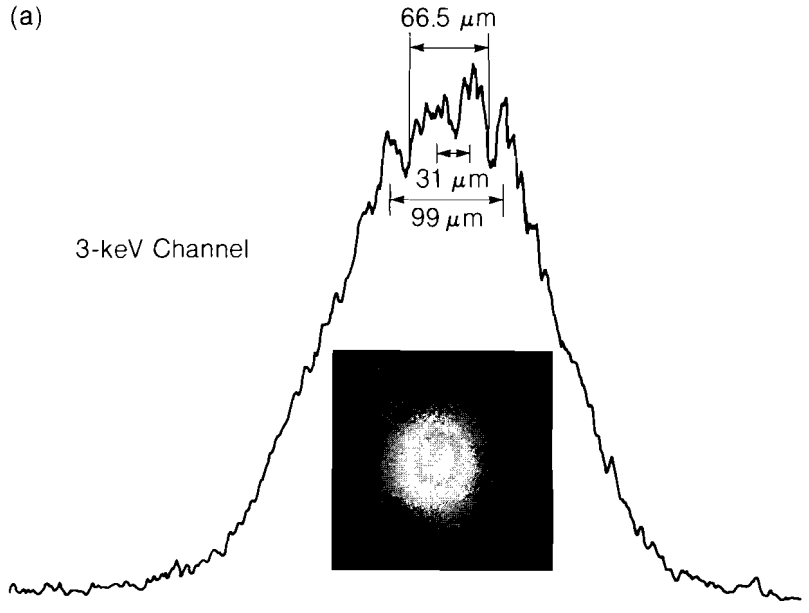

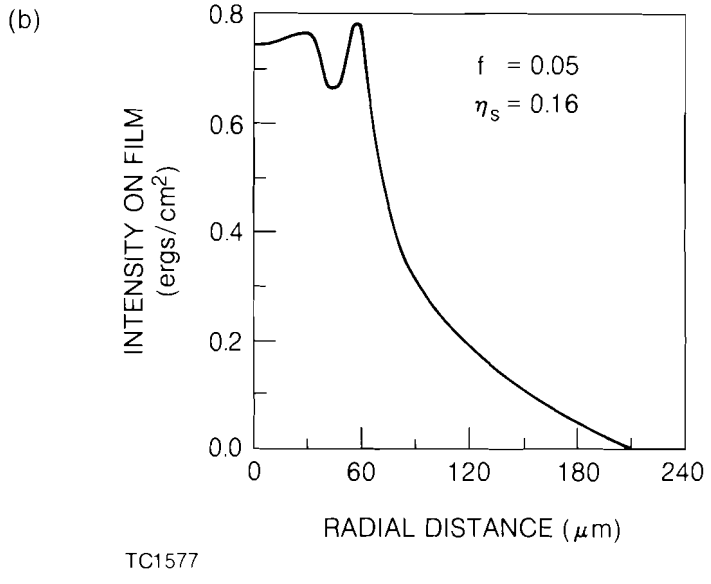

Fig. 20.17
X-ray microscope image for shot 7035: (a) experimental, (b) simulated.

stationary heat front when the pusher stagnates. The region from which the strong x-ray emission originates is narrow and corresponds to an optimum combination of electron temperature and density in the heat front. The integrated energy from that emission is usually small and does not show up in microscope images because the emitting

region moves continuously during the implosion. When the pusher stagnates, the density of the pusher increases slightly and the emitting region remains stationary long enough to produce a ring in the microscope image. Figure 20.18 plots the spatial distribution of x-ray emission from the pusher at various times near stagnation. Early in time, before stagnation, only the ring structure associated with the heat front can be seen. At stagnation the inner surface of the glass also becomes stationary and more dense and dominates the streak image. A short time later, it has cooled and again the ring associated with the heat front, which is still hot, dominates the image. The integration of these streak images over time leads to the double-ring microscope image observed in the experiment.

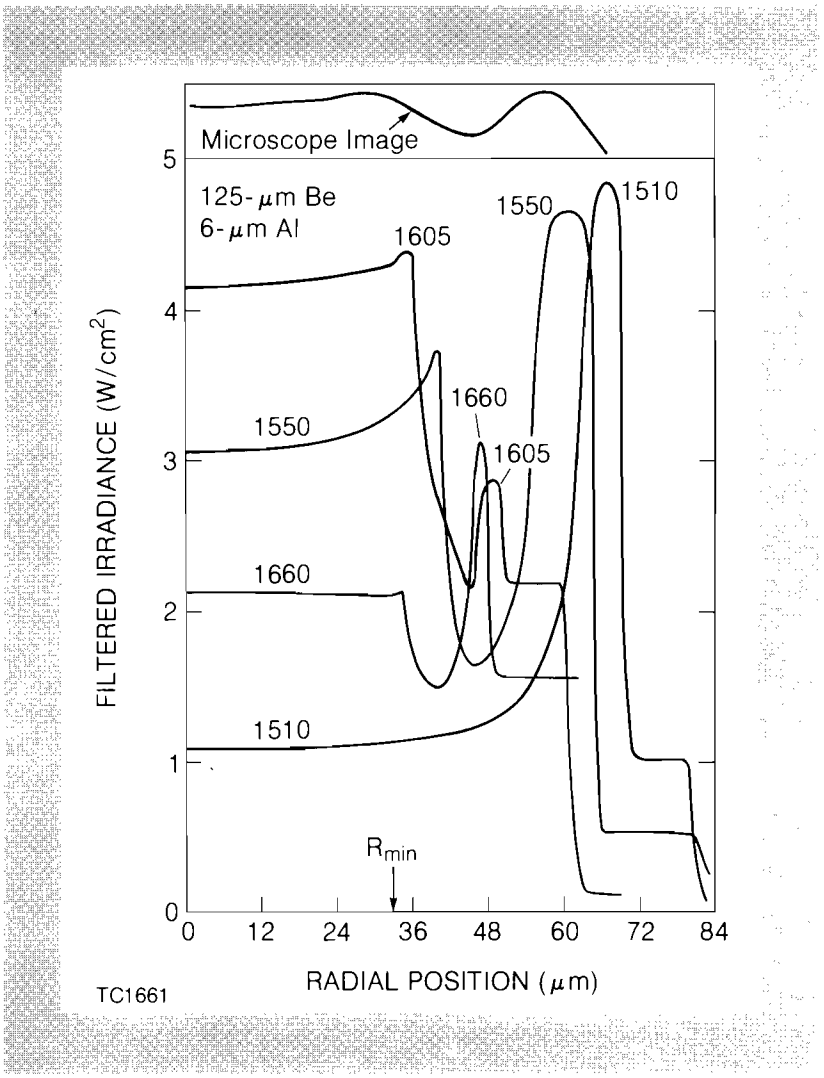

Fig. 20.18
Several frames of the x-ray emission from the target during stagnation. X-ray microscope images plotted above for reference.

The presence of the ring structure in the x-ray microscope images is sensitive to the two free parameters in the simulation: the flux limiter and the fraction of the absorbed energy that goes into the suprathermal electron component η_s. A caveat for the analysis is that the simulated microscope images are obtained from x-ray emission calculated from LTE (local thermal equilibrium) opacity tables. Non-LTE emission usually yields lower x-ray intensities because of the

ionization lag when the temperature increases rapidly. The effect may be more important in the production of the outer ring because the heat front moves rapidly through the cold glass. On the other hand, the material on the inner part of the glass is continuously heated to emission temperatures over a longer time and, therefore, may have a better chance to reach LTE conditions. Also, the code-calculated images are for the incident intensity on the film rather than for the film density; the film response will tend to reduce the apparent intensity differences in the core region, but not the shape, because of exposure saturation.

Figure 20.19 shows the x-ray microscope images calculated by *LILAC* for several values of f and η_s; the images are for a given filter combination (6 μm of Al and 125 μm of Be). Code results show that the greater the thickness of the Be foil, the higher the emission from the outer ring with respect to that of the inner core. The experimentally observed microscope images show the weak ring structure for all three filter combinations. Two general observations can be made. First, the larger the flux limiter, the weaker the outer ring emission is with respect to the inner core emission; second, the larger the absorbed energy in suprathermal electrons, the weaker the emission from the core structure.

The combinations of f and η_s which yield a weak ring between an outer emitting ring and a core structure are those of Figs. 20.19(b) and 20.19(d) in which f = 0.03 and 0.05, respectively, and η_s = 0.16. The ring in Fig. 20.19(c) is probably too weak to record photographically. The weak/strong ring structure does not exist for the other filter combinations. For the larger flux limiter, f = 0.08, the weak/strong ring structure does not exist; it is doubtful that non-LTE effects would lead to the experimentally observed structure since they would weaken an already inconsequential outer ring. In Fig. 20.19(a), no inner structure is seen; in this case the non-LTE effects could reduce the emission from the outer ring enough to let the inner core structure appear. For all values of the flux limiter, doubling the energy absorbed into the suprathermal electrons reduces the intensity of the inner ring to a point where it almost disappears.

Two conclusions can be drawn from the simulation. First, the flux limiter which provides the best description of implosion experiments is less than 0.08 and most likely larger than 0.03. This result agrees with those of the planar transport experiment at 351 nm and with the flux limiter required to model the burn-through to a titanium substrate in the spherical transport experiments at 1054 nm. Second, the fraction absorbed into the suprathermal electron component must be less than 20% of the total absorbed energy.

This places an upper limit on the preheat level in the pusher during the implosion. With η_s = 0.16 the glass is preheated to less than 100 eV during the implosion. This preheat level is much lower than that required in the spherical transport experiment to explain the large burn-through in plastic to the aluminum substrate, and other mechanisms must be sought to explain the aluminum emission.

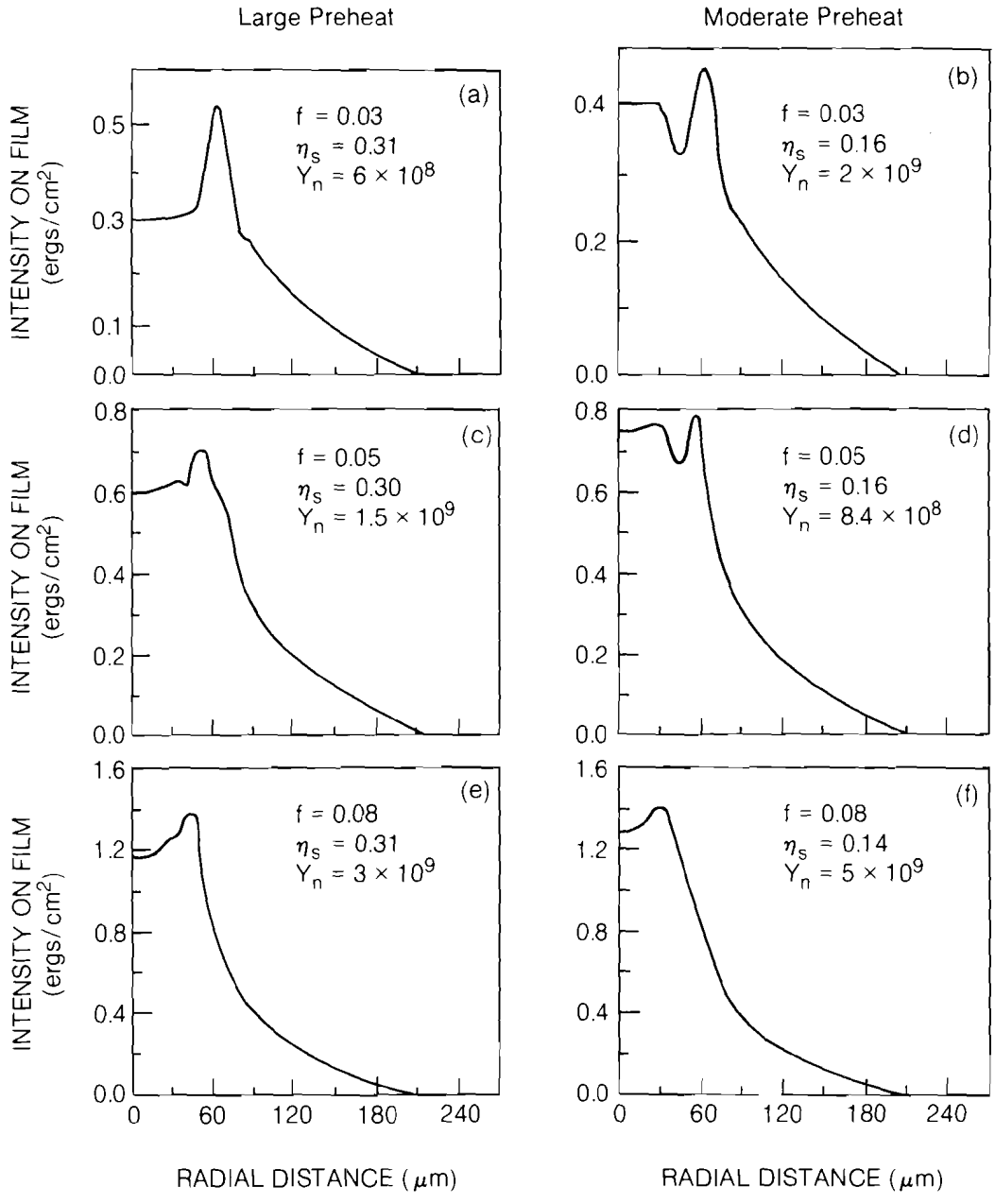

Fig. 20.19
X-ray microscope image for three values of the flux-limiter and two values of the absorbed energy in the suprathermal electron component.

ACKNOWLEDGMENT

This work was supported by the U.S. Department of Energy Office of Inertial Fusion under contract number DE-AC08-80DP40124 and by the Laser Fusion Feasibility Project at the Laboratory for Laser Energetics which has the following sponsors: Empire State Electric Energy Research Corporation, General Electric Company, New York State Energy Research and Development Authority, Northeast Utilities Service Company, Ontario Hydro, Southern California Edison Company, The Standard Oil Company, and University of Rochester. Such support does not imply endorsement of the content by any of the above parties.

REFERENCES

1. L. Spitzer and R. Harm, *Phys. Rev. Lett.* **89**, 977 (1953).
2. D. R. Gray and D. J. Kilkenny, *Plasma Phys.* **22**, 81 (1980).
3. W. C. Mead *et al.*, *Phys. Fluids* **27**, 1301 (1984).
4. B. Yaakobi, T. Boehly, P. Bourke, Y. Conturie, R. S. Craxton, J. Delettrez, J. M. Forsyth, R. D. Frankel, L. M. Goldman, R. L. McCrory, M. C. Richardson, W. Seka, D. Shvarts, and J. M. Soures, *Opt. Commun.* **39**, 175 (1981).
5. T. J. Goldstack *et al.*, *Phys. Fluids* **25**, 1634 (1982).
6. B. Yaakobi, J. Delettrez, L. M. Goldman, R. L. McCrory, R. Marjoribanks, M. C. Richardson, D. Shvarts, S. Skupsky, J. M. Soures, C. P. Verdon, D. M. Villeneuve, T. Boehly, R. Hutchison, and S. Letzring, *Phys. Fluids* **27**, 516 (1984).
7. W. L. Kruer, LLNL Report UCRL-81896 (1978).
8. D. R. Welch, D. B. Harris, A. H. Bennish, and G. H. Miley (pre-publication manuscript).

Section 3
ADVANCED TECHNOLOGY DEVELOPMENTS

3.A Lasers in Angioplasty

The condition known as hardening of the arteries or atherosclerosis is the blockage of the arteries by plaque. When 80-90% of the cross-sectional area of a coronary artery is occluded, the flow of blood is seriously impaired and the risk of cardiac arrest is considerably increased. Figure 20.20 is a photograph of some actual arterial occlusions.

Presently, there are several operations that may be performed to restore blood flow in occluded arteries. One of these—arterial bypass surgery—is one of the most commonly performed operations in the United States today. In bypass surgery, arterial grafts are made to reroute blood flow around blockages. Another procedure, endarterectomy, is used especially to excise blockages from the carotid arteries.[1] In this procedure blood flow is blocked in the area, the artery is opened longitudinally, and the plaque is "peeled" from the artery wall. Then, the artery is reclosed and blood flow is restored.

These are long operations that pose moderate to high risk to the patient, and they are expensive to perform. Postoperative recovery periods are lengthy and often painful. Accordingly, there is continuing interest in developing more attractive alternative treatments for arterial blockages.

In this respect the laser has attracted a great deal of interest recently as the key instrument in a surgical system to treat arterial

E3258

Fig. 20.20
Photograph of cross-sections of human arteries showing various degrees of occlusion due to atherosclerosis.

occlusions. In concept this system channels high-intensity laser radiation through a small optical fiber to burn away the occlusion. The optical fiber is combined with an endoscope for monitoring the process and delivered to the occlusion site through a four-port catheter, introduced into the body through a small shoulder or groin incision and threaded along the arterial passageways. The other two ports will be used for local blood-flow blockage and for suction and flushing. The diameter of the entire catheter device must be less than 2 mm.

Before laser surgery can be performed in a clinical setting, or even on a laboratory animal, it is necessary to determine the effects of laser radiation on arterial plaque and on healthy tissue as well as complete the development of the system described above. We have carried out and documented tissue-irradiation tests here on samples of plaque and healthy tissue. Documentation includes both photographic records and histological analysis. Damage thresholds have been determined for direct irradiation from the laser source and for radiation delivered through an optical fiber.

For direct exposures, laser light was focused onto the specimen with a long focal length lens at an angle of incidence of approximately 60°. For fiber exposures a microscope objective was used to couple the laser light into a 100- to 200-μm-diameter quartz fiber. The fiber output tip was brought to within 2 mm or less of the specimen at an angle of 90° to the surface.

During preliminary direct-exposure tests, we observed that a 514-nm, argon-ion laser operated at a power output of 3-W cw was much more effective on plaque specimens than a similarly focused, 1064-nm, mode-locked, Nd:YAG laser operated at 7-W output. For this reason only the argon-ion laser was used for subsequent testing.

Atherosclerotic plaque is a result of cholesteric deposits on artery walls. Four types of plaque are found in human arteries. Fatty streak

plaque is soft and yellowish. Subintimal calcified plaque is a hard deposit under the artery surfaces, the intima. Calcified plaque is a hard deposit on the artery wall. Complicated plaque is calcification on the artery with ulcers and craters and coagulated blood called thrombus underneath the surface.

Damage thresholds were different for the four kinds of plaque. For specimens submerged in distilled water, the focused argon-ion-laser damage thresholds for direct exposure were found to be 9.6×10^3 W/cm^2 for fatty streak plaque, 1.3×10^4 W/cm^2 for subintimal calcified plaque, and 1.4×10^4 W/cm^2 for calcified plaque and complicated plaque. The damage threshold for healthy aortic tissue was 8.5×10^3 W/cm^2.

When calcified plaque was contacted by a 200-μm-diameter optical fiber, the damage threshold was lower—2.5×10^3 W/cm^2. When the fiber tip was pulled back from the specimen, however, the illumination spot spread out, reducing the intensity. As a result, it was necessary to raise the laser power and increase the exposure time in order to damage the plaque.

To evaluate the damage to plaque for different exposure times and conditions, an investigation was carried out on an atherosclerotic aorta which was cut into four longitudinal strips. Two strips were exposed to focused laser light directly, one dry and one submerged in saline solution. The other strips were exposed to laser light delivered by an optical fiber, one dry and one submerged in saline solution. Power was held constant in all cases while time was varied. Each site was photographed and analyzed histologically (Fig. 20.21).

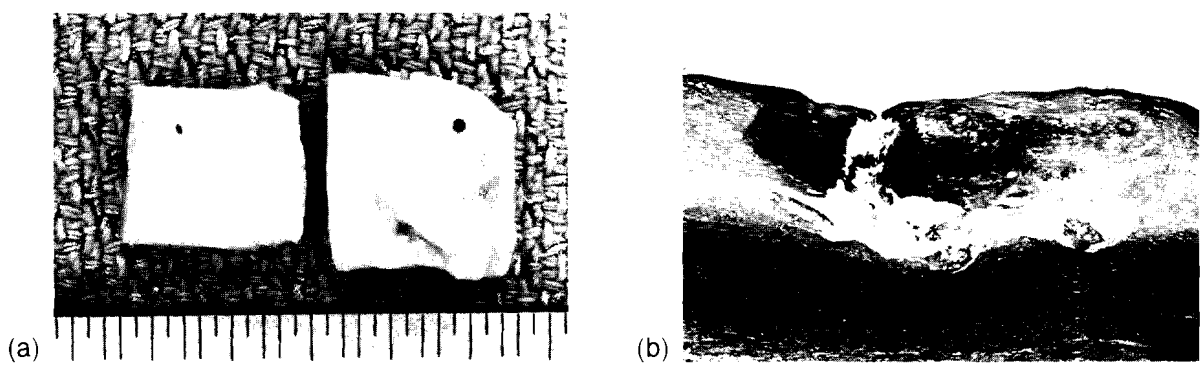

Fig. 20.21
Details of laser tests on atherosclerotic aorta samples:
(a) Photograph of irradiated samples.
(b) Photomicrograph of section of laser crater.

When a fiber was used for delivering light, it was at a 90° angle to the specimen. In actual surgery, unless there is a total, or near total, occlusion, the fiber will be at shallower angles. In order to see the effects of different delivery angles on the plaque, exposures were made at several angles of incidence. Exposure time and power out of the fiber were held constant. Each site was photographed and will be analyzed histologically.

Next, the difference in damage due to light delivered by a cut fiber tip and a rounded fiber tip was considered. Submerged plaque was exposed for times varying from 2-10 minutes. Twelve exposures were

done in all, six with delivery by a cut tip and six with delivery by a rounded tip. Each site was photographed and will be analyzed histologically.

Histological slides of dry-state, direct exposures show that much less power is needed to do the same amount of damage in a dry state than in a wet state. For exposure times ranging from 1-60 s, destruction was confined to the plaque layer [Fig. 20.21(a)]. A 60-s exposure showed complete penetration of a 2-mm layer of plaque, but no destruction of healthy aortic tissue underneath the plaque. At an exposure time of 2 min, we began to see penetration of the healthy aortic wall. At 4-6 min there was complete penetration of the artery wall. No further histological analyses have been completed at this time.

When removing plaque from coronary arteries on the heart wall, it may not be possible to maneuver the entire catheter into those arteries due to restrictions on size and flexibility of the catheter. Therefore, the negotiability of coronary arteries with an optical fiber was investigated using the heart of a pig. A pig's heart was chosen as a model because it is similar to the human heart.

To negotiate the coronary arteries, sharp turns of almost 90° must be made by the fiber shortly after entering the arteries from the aorta. A 200-μm quartz fiber was found to be too rigid to make these turns easily. A 125-μm quartz fiber, on the other hand, was found to be very flexible and easily capable of making the sharp turns. Later, negotiation of coronary arteries will be practiced with a new 1.5-mm endoscope. It will only be necessary to maneuver a fiber and endoscope 3-5 cm into the arteries since occlusions occur most frequently at the forks of the vessels and other areas of turbulent flow (Fig. 20.22). Once the fiber has been maneuvered into the coronary arteries, plaque buildups must be identified with the endoscope. When the plaque is identified, the laser will be turned on and the plaque destroyed. Should the endoscope prove to be too large or too inflexible to negotiate the twists and turns of the coronary arteries, the fiber's progress through the coronary arteries may have to be watched using ultrasound imaging.

Although the 125-μm fiber is flexible enough to negotiate the arterial pathways, it is probable that some sort of guidance system will be necessary to accomplish this. A guide wire attached very near the end of the fiber could be used for steering, but this makes the fiber tip rigid and bulky. Another difficulty in maneuvering is the square edges of the fiber which catch and grab the artery walls. This not only makes it much more difficult to maneuver the fiber, but it also increases the danger of perforating the artery wall. To help the fiber maneuver more smoothly, the end was rounded using an oxygen-acetylene torch. The rounded end moves more smoothly through the coronary arteries and also helps focus the emerging light. This makes lesioning plaque more efficient since energy is not wasted doing inadvertent damage to surrounding tissues.

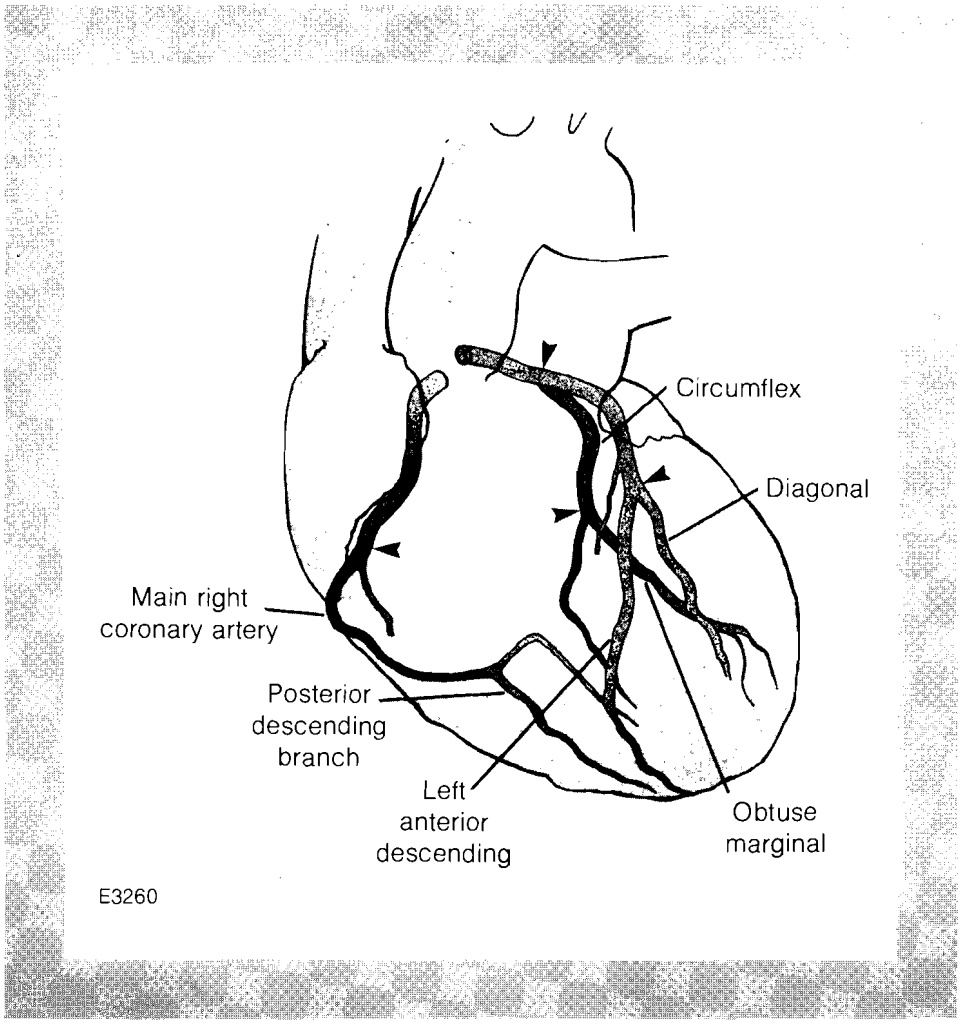

Fig. 20.22
Usual locations of occlusions in coronary arteries.

We conclude that it is feasible to destroy atherosclerotic plaque using an argon-ion laser with an optical fiber for delivery with 3 W or less of laser power. The Nd:YAG laser showed no plaque damage at 7-W output; higher power was not investigated. The wet-state damage thresholds were found to be between 8.5×10^{3} W/cm^2 and 1.4×10^{4} W/cm^2 at 514 nm. An absorption spectrum of a solution of 1.748×10^{-2} M plaque (dissolved in chloroform) indicates that 450 nm is near the optimum wavelength for plaque destruction. The threshold of damage of plaque was not found to be more than 1.4×10^{4} W/cm^2; however, at the same power level, removal of blockages would have taken an inordinate amount of time. The use of higher power as well as shorter wavelengths will be investigated in the near future. Actual laser surgery on animals is also planned for the near future. Once the optimum techniques are found for the removal of arterial plaque, and the patient's safety is guaranteed, this new laser surgical procedure can be performed on humans. At first, procedures will be confined to larger arteries, such as the aorta and the carotid, and femoral arteries. It will not be possible to remove plaque from small coronary arteries until the equipment has been miniaturized. Hopefully, lasers combined with fiber delivery systems will be used clinically to remove arterial plaque in 6-12 months.

ACKNOWLEDGMENT

This work was supported by the following sponsors of the Laser Fusion Feasibility Project at the Laboratory for Laser Energetics—Empire State Electric Energy Research Corporation, General Electric Company, New York State Energy Research and Development Authority, Northeast Utilities Service Company, Ontario Hydro, Southern California Edison Company, The Standard Oil Company, and University of Rochester. Such support does not imply endorsement of the content by any of the above parties.

This work was the result of a collaboration between LLE and The University of Rochester Medical Center's Department of Cardiovascular Surgery. Valuable suggestions and contributions to the project have been made by Dr. Robert Frankel, Dr. George L. Hicks, Dr. Philippe Bado, and Dr. Pierre Tibi.

REFERENCES

1. G. Van Stiegmann, D. Kahn, A. G. Rose, P. C. Bornman, and J. Terblanche, "Endoscopic Laser Endarterectomy," *Surgery, Gynecology and Obstetrics* **158**, 529-534 (1984).
2. Robert H. Anderson and Anton E. Becker, *Slide Atlas of Cardiac Surgery, Vol. 7, Clinical Cardial Anatomy I*, p. 5.

3.B A New Engineering Damage Criterion for Thin-Film Optical Coatings

Laser damage tests are usually carried out to monitor quality control for established thin-film coating designs or to gauge optical survival potential for new, experimental coating designs. The procedure widely followed in laser damage tests is a one-on-one test regimen. That is, each sample site is irradiated only once, and the occurrence or non-occurrence of damage is monitored immediately after irradiation. Changing the irradiation fluence as one sample site after another is irradiated allows us to find a sample's average damage threshold. This average is often determined by splitting the difference between the highest fluence which any sample site survived without showing damage and the lowest fluence which did cause damage. Repeating this procedure for many identical samples yields an average damage threshold for a given coating design and a corresponding standard deviation. Both are obtained in conventional, statistical fashion.

One reason for carrying out damage tests in this manner is the long-standing problem in maintaining constant laser-intensity profiles both spatially and temporally within the irradiation volume. As a consequence of pulse-to-pulse laser-output fluctuations, it was recognized that multiple irradiations of a sample site made a meaningful interpretation of damage results virtually impossible. Single irradiation of each sample site therefore became a necessity.[1]

This strictly instrumental restriction puts severe limits on the utility of one-on-one damage-test results obtained. For what can ultimately be inferred from these data is that for a given coating design, the fluence on the first shot should not exceed a certain threshold value,

if damage is to be avoided. Very few laser systems are, however, intended for just a single-shot useful life. To predict from these data, laser-system component performance over many shots requires two important assumptions. First, the status of the component can be in only one of two states, undamaged or damaged. Moreover, the undamaged state is required to remain entirely constant during all irradiations up to the damaging event. These assumptions deserve some scrutiny.

We have recently started to monitor both the conventional one-on-one average damage threshold and the multiple irradiation behavior of sites. These tests were carried out on polymer-oxide-AR surface structures on fused SiO_2. These coatings exhibit peculiar damage morphologies which are especially suitable for such tests (see Fig. 20.23). Damage manifests itself there in an orange-peel pattern of hundreds of small scattering centers separated from one another by much larger distances than their average size. The larger of these damage sites can be detected by the unaided eye. From a practical viewpoint, only such damage sites are detected in the field during routine maintenance inspection of large optical components. Unless such evidence appears, a component is normally judged fit for further use. Appearance of such damage sites could therefore be termed an engineering damage criterion. This differs from the conventional damage criterion in which the appearance of a single, additional scattering center within the irradiated volume is counted as evidence of damage. A single scattering center can be observed only under high-resolution microscopy.

G1501

Fig. 20.23
Typical polymer-oxide "orange-peel" damage morphology after large-spot irradiation by 1-ns, 351-nm laser pulse (magnification 110X).

Our method of experimentally distinguishing single-center, conventional damage from engineering damage also sheds light on the issue of damage-initiation versus damage-propagation thresholds. Experiments at Los Alamos[2] showed that new scattering centers observed after a first irradiation neither multiply nor grow in size upon subsequent irradiation at constant fluence. Significantly higher fluences were required to cause added damage to such pre-irradiated sample areas. No explanation was available for this phenomenon.

The most important finding of the LLE multiple-irradiation tests is the sample-hardening effect. Repetitive irradiation with slowly increasing laser fluences makes sample sites survive final fluence levels which, without exception, cause other sites on the same sample to suffer massive damage on first irradiation. A pattern emerges from these measurements in which the hardening of sites depends critically on the rate at which the fluence is raised from shot to shot. Yet the hardening does not seem to depend on the shot-to-shot stability of the laser's spatial intensity distribution. For polymer-oxide coatings, fluence increases exceeding 42% cause engineering damage. This happens irrespective of the absolute fluence level from which the increase occurs as long as that level lies above 1.5 J/cm^2. Below this level, increases of 100% or more are of no consequence.

Damage evolution on a typical, hardened site proceeds in three stages. During low-fluence initial irradiation, very few scattering centers are created, indicative for one-on-one damage. No new or enlarged existing centers are noticed through successive irradiations of slowly raised fluence until an excessive laser-intensity fluctuation in the upper fluence range causes massive engineering damage. Although the cause for the initial few-scatter damage is not known, it is likely to be different from that for the massive damage. The absence of progressive damage after first irradiation casts doubt on the significance of the early-damage mechanisms and thereby on the whole one-on-one damage evaluation itself.

The microscopic process of hardening is currently not understood. We observe that samples with one-on-one damage thresholds near 1 J/cm^2 will sustain fluence levels above 3.5 J/cm^2 after hardening. Limited evidence indicates the possible existence of a critical hardening path for polymer-oxide coatings. If that path were known, all sample sites could be treated in a similar, controlled fashion. Further insight into the detailed hardening mechanism could be gained. Also, a logically consistent N-on-one damage threshold could be constructed.

In the absence of a well-analyzed critical path, we assume that limited deviation from such a path can be tolerated and that our narrow data base permits the derivation of such an N-on-one damage threshold. In Fig. 20.24 the traditional one-on-one average damage threshold for three polymer-oxide samples is compared with N-on-one thresholds obtained from the same samples. The marked improvement due to hardening is evident.

Answers to several questions are currently being sought:

- Is the hardening path linear or non-linear?
- Does low-fluence pretreatment also affect one-on-one thresholds?
- Can hardening procedures be devised which prepare polymer-oxide coatings to meet given, specific design requirements?

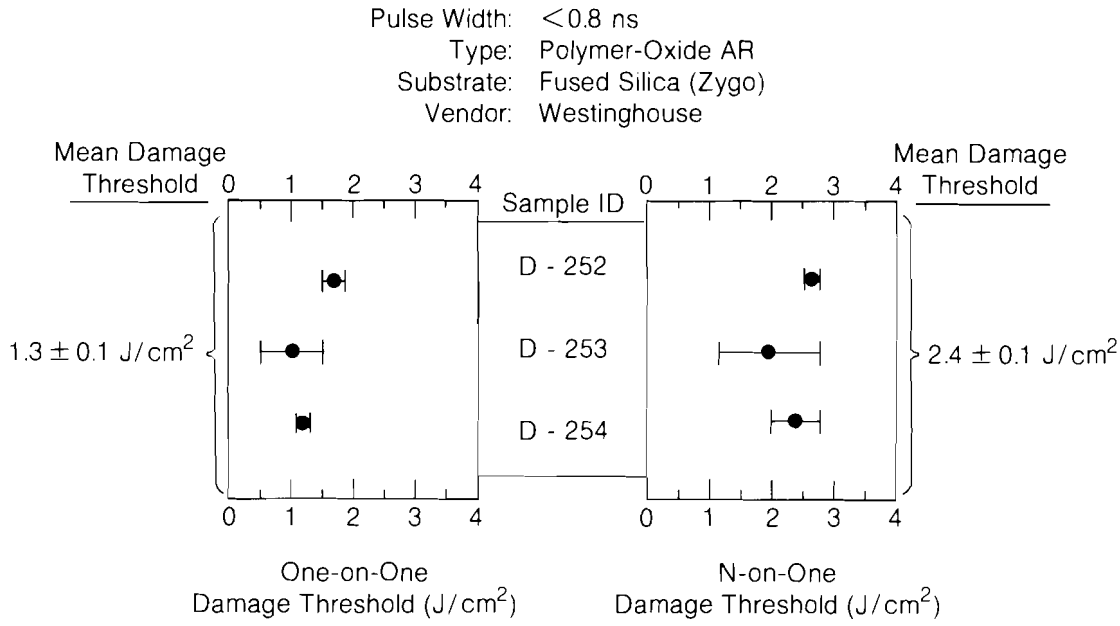

Fig. 20.24
Composition of single-shot and N-on-one average damage thresholds for selected polymer-oxide samples.

ACKNOWLEDGMENT

This work was supported by the U.S. Department of Energy Office of Inertial Fusion under contract number DE-AC08-80DP40124 and by the Laser Fusion Feasibility Project at the Laboratory for Laser Energetics which has the following sponsors: Empire State Electric Energy Research Corporation, General Electric Company, New York State Energy Research and Development Authority, Northeast Utilities Service Company, Ontario Hydro, Southern California Edison Company, The Standard Oil Company, and University of Rochester. Such support does not imply endorsement of the content by any of the above parties.

We are indebted to Dr. Deborah Partlow of Westinghouse Research and Development Center, Pittsburgh, PA, for preparing the polymer-oxide coatings.

REFERENCES

1. For further information on damage-testing procedures consult the various volumes of *Proceedings of the Annual Symposium on High-Power Laser Optical Materials* published by the Government Printing Office for the National Bureau of Standards.
2. Steven Foltyn (private communication).

Section 4
NATIONAL LASER USERS FACILITY NEWS

This report covers the activities of the National Laser Users Facility (NLUF) during the quarter 1 July to 30 September 1984. During this period two users conducted experiments on LLE facilities. In addition, preparation for next year's steering committee meeting has begun, including solicitation of proposals.

In the user experiment on the GDL system, 351-nm laser light was focused onto thin-foil targets to study the Raman spectra and hot-electron emission spectra. The participating individuals in this experiment are

- **Chan Joshi**, **Humberto Figueroa**, and **Chris Clayton** (University of California, Los Angeles): "Studies of the Two-Plasmon Decay and Stimulated-Raman-Scattering Instabilities in Long-Scale-Length Plasmas."

The user experiment on the OMEGA system was the study of time-resolved thermal transport with six beams of 351-nm light focused onto spherical targets.

- **Burton L. Henke** and **Paul A. Jaanimagi** (University of Hawaii at Manoa): "Evaluation and Application of a Streak Camera and Photographic Camera Coupled Elliptical-Analyzer Spectrograph System for the Diagnostics of Laser-Produced X-Ray Sources (100-10,000-eV Region)."

Additional information on these experiments can be obtained from the scientists associated with the experiment.

The users facility will be accepting proposals until 1 February 1985 — the deadline for proposal submission. A description of the users facility and funding opportunities is included below.

The users facility is available for experiments requiring high-intensity laser beams. Users have access to both the OMEGA and GDL facilities. Fundamental studies center around applications in high-energy-density physics. High-energy-density physics experiments utilize an intense pulse of laser light focused to a diameter of approximately 10^{-3} cm. A solid material irradiated by such an intense laser pulse rapidly becomes an ionized gas, or plasma, with a temperature of 50 million degrees. This point-source plasma thus provides the necessary conditions for studies of thermonuclear fusion, spectroscopy of highly ionized atoms, shock waves, laboratory astrophysics, or the fundamental physics of matter under high intensities.

The University of Rochester operates the users facility under agreement with the United States Department of Energy. The Department of Energy funds the operation of the users facility thus making it possible for researchers to conduct experiments without direct charge. In addition the Department of Energy provides research funds directly to users. However, these fields are limited to laser fusion, plasma physics, and associated applications. User proposals in other areas can be accepted; however, funding support for both operations and research activities must be obtained separately through other agencies (e.g., the National Science Foundation).

All proposals are reviewed by the National Laser Users Facility Steering Committee which ranks them according to scientific merit. The terms of appointment for members are staggered so that part of the membership is renewed annually. The steering committee meets annually and makes its recommendations after reviewing proposals.

Following a steering committee meeting, researchers are advised of the committee's recommendation. For approved proposals, information will be sent regarding submission of the proposal to the Department of Energy in order to qualify for user funds. The Department of Energy will take into account steering committee recommendations for allocation of user funds.

For more information about proposal guidelines and the resources available at the users facility, please contact

Thomas C. Bristow, Manager
National Laser Users Facility
Laboratory for Laser Energetics
University of Rochester
250 East River Road
Rochester, New York 14623
(716) 275-2074

ACKNOWLEDGMENT

This work was supported by the U.S. Department of Energy Office of Inertial Fusion under contract number DE-AC08-80DP40124.

PUBLICATIONS AND CONFERENCE PRESENTATIONS

Publications

D. Agassi, "Phenomenological Model for Picosecond-Pulse Laser Annealing of Semiconductor," *J. Appl. Phys.* **55**, 4376-4383 (1984).

R. S. Craxton and R. L. McCrory, "Hydrodynamics of Thermal Self-Focusing in Laser Plasmas," *J. Appl. Phys.* **56**, 108-117 (1984).

J. M. Forsyth and R. D. Frankel, "Experimental Facility for Nanosecond Time-Resolved, Low-Angle X-Ray Diffraction Experiments Using a Laser-Produced Plasma Source," *Rev. Sci. Instrum.* **55**, 1235-1242 (1984).

N. S. Murthy and H. Kim. "Molecular Packing in Alkylated and Chlorinated Poly-p-xylylenes," *Polymer* **25**, 1093-1096 (1984).

W. Seka, E. A. Williams, R. S. Craxton, L. M. Goldman, R. W. Short, and K. Tanaka, "Convective Stimulated Raman Scattering Instability in UV Laser Plasmas," *Phys. Fluids* **27**, 2181-2186 (1984).

K. Tanaka, W. Seka, L. M. Goldman, M. C. Richardson, R. W. Short, J. M. Soures, and E. A. Williams, "Evidence of Parametric Instabilities in Second Harmonic Spectra from 1054-nm Laser-Produced Plasmas," *Phys. Fluids* **27**, 2187-2190 (1984).

Forthcoming Publications

J. A. Abate, A. W. Schmid, M. J. Guardalben, D. J. Smith, and S. D. Jacobs, "Characterization of Micron-Sized, Optical Coating Defects by Photothermal Deflection Microscopy," to be published in *Proceedings of the 15th Annual Symposium on Optical Materials for High Power Lasers*.

W. E. Behring, J. F. Seely, S. Goldsmith, L. Cohen, M. C. Richardson, and V. Feldman, "Transitions of the Type 2s-2p in Highly Ionized Zn, Ga, and Ge," accepted for publication by *Journal of the Optical Society of America*.

H. L. Helfer, R. L. McCrory, and H. M. Van Horn, "Further Monte Carlo Calculations for the Classical One-Component Plasma in the Range $100 \leq \Gamma \leq 160$: The FCC Lattice," accepted for publication by *Journal of Statistical Physics*.

S. Kacenjar, L. M. Goldman, A. Entenberg, and S. Skupsky, "$<\rho R>$ Measurements in Laser-Produced Implosions Using Elastically Scattered Ions," accepted for publication by *Journal of Applied Physics*.

R. Keck, L. M. Goldman, M. Richardson, W. Seka, and K. Tanaka, "Observation of High Energy Electron Distributions in Laser Plasmas," accepted for publication by *Physical Review*.

E. L. Lindman and K. Swartz, "Some Applications of the Hot Electron Transport Equation," to be published in the *1983 Proceedings for the CECAM Workshop on 'The Flux Limiter and Heat Flow Instabilities in Laser-Fusion Plasmas.'*

C. J. McKinstrie, A. Simon, and E. A. Williams, "Nonlinear Saturation of Stimulated Raman Scattering in Homogeneous Plasma," accepted for publication by *Physics of Fluids*.

G. A. Mourou and K. E. Meyer, "Subpicosecond Electro-Optic Sampling Using Coplanar Strip Transmission Lines," accepted for publication by *Applied Physics Letters*.

A. Schmid, D. Smith, M. Guardalben, and J. Abate, "Photothermal-Deflection Analysis of UV Optical Thin Films," accepted for publication by *SPIE Volume 476, Technical Symposium East—Excimer Lasers, Their Applications and New Frontiers in Lasers*.

J. M. Soures, review of *The High-Power Iodine Laser*, by G. Brederlow, E. Fill, and K. J. Witte, accepted for publication by *Journal of Quantum Electronics*.

M. Strauss, G. Hazak, D. Shvarts, and R. S. Craxton, "Magnetic-Field Effects on Electron Heat Transport in Laser-Produced Plasmas," accepted for publication by *Physical Review A*.

K. Tanaka, L. M. Goldman, W. Seka, R. W. Short, and E. A. Williams, "Spectroscopic Study of Scattered Light at Around the Fundamental Wavelength in UV Laser-Produced Plasmas," accepted for publication by *Physics of Fluids*.

B. Yaakobi, "X-Ray Lithography Using Laser Plasma as a Source," accepted for publication by *Solid State Technology*.

Conference Presentations

H. Kim, S. D. Jacobs, and K. A. Cerqua, "Liquid-Crystal Laser-Blocking Filters," presented at the Thirteenth Congress of the International Commission of Optics, Sapporo, Japan, August 1984.

R. L. McCrory, O. Barnouin, R. S. Craxton, J. Delettrez, R. Epstein, L. Forsley, L. M. Goldman, R. J. Hutchison, R. L. Keck, H. Kim, W. Lampeter, S. A. Letzring, R. S. Marjoribanks, P. McKenty, M. C. Richardson, W. Seka, R. W. Short, A. Simon, S. Skupsky, J. M. Soures, K. Swartz, K. Tanaka, C. Verdon, and B. Yaakobi, "Short-Wavelength, Direct-Drive Laser Fusion at the Laboratory for Laser Energetics," presented at the Tenth International Conference on Plasma Physics and Controlled Nuclear Fusion Research of the International Atomic Energy Agency, London, England, September 1984.

The work described in this volume includes current research at the Laboratory for Laser Energetics which is supported by Empire State Electric Energy Research Corporation, General Electric Company, New York State Energy Research and Development Authority, Northeast Utilities Service Company, Ontario Hydro, Southern California Edison Company, The Standard Oil Company, University of Rochester, and the U.S. Department of Energy Office of Inertial Fusion under contract DE-AC08-80DP40124.